The peptidoglycan of Borrelia burgdorferi can persist in discrete tissues and cause systemic responses consistent with chronic illness

Article *in* Science Translational Medicine · April 2025

DOI: 10.1126/scitranslmed.adr2955

9 authors, including:

Osamudiamen Ebohon
Michael and Cecilia Ibru University
22 PUBLICATIONS **140** CITATIONS
SEE PROFILE

Robert Lochhead
Medical College of Wisconsin
29 PUBLICATIONS **576** CITATIONS
SEE PROFILE

Carmen Jane Booth
Yale University
153 PUBLICATIONS **13,652** CITATIONS
SEE PROFILE

Brandon Jutras
Virginia Tech
48 PUBLICATIONS **1,519** CITATIONS
SEE PROFILE

LYME DISEASE

The peptidoglycan of *Borrelia burgdorferi* can persist in discrete tissues and cause systemic responses consistent with chronic illness

Mecaila E. McClune[1,2,3,4], Osamudiamen Ebohon[1,2,3,4], Jules M. Dressler[3,4], Marisela M. Davis[3], Juselyn D. Tupik[4,5], Robert B. Lochhead[6], Carmen J. Booth[7], Allen C. Steere[8], Brandon L. Jutras[1,2,3,4,9]*

Persistent symptoms after an acute infection is an emerging public health concern, but the pathobiology of such conditions is not well understood. One possible scenario involves the persistence of lingering antigen. We have previously reported that patients with postinfectious Lyme arthritis often harbor the peptidoglycan (PG) cell wall of *Borrelia burgdorferi*, the Lyme disease agent, in the synovial fluid of their inflamed joints after treatment. However, it is not yet known how *B. burgdorferi* PG persists, in what form, or if it may play a role in other postinfectious complications after Lyme disease. Using a murine model, we developed a real-time in vivo system to track *B. burgdorferi* PG as a function of cell wall chemistry and validated our findings using both molecular and cellular approaches. Unlike typical bacterial PG, the unique chemical properties of polymeric *B. burgdorferi* PG drive murine liver accumulation, where the cell wall material persists for weeks. Kupffer cells and hepatocytes phagocytose and retain *B. burgdorferi* PG and, although liver occupancy coincides with minimal pathology, both organ-specific and secreted protein profiles produced under these conditions bear some similarities to reported proteins enriched in patients with chronic illness after acute infection. Moreover, transcriptomic profiling indicated that *B. burgdorferi* PG affects energy metabolism in peripheral blood mononuclear cells. Our findings provide mechanistic insights into how a pathogenic molecule can persist after agent clearance, potentially contributing to illness after infection.

INTRODUCTION

Nearly half a million people are thought to acquire Lyme disease each year in the United States (*1*, *2*). Upon transmission from an infected *Ixodes* spp. tick, the spirochetal pathogen *Borrelia burgdorferi* rapidly disseminates and may cause a multisystem disorder if left untreated. Most patients are effectively treated with doxycycline and return to health, but ~15% do not and instead develop posttreatment Lyme disease syndrome (PTLDS) (*3*, *4*). PTLDS is defined as symptoms lasting for more than 6 months after recommended treatment (*5*, *6*). Patients with PTLDS often report similar symptoms such as chronic fatigue, diffuse pain, and neurocognitive issues (*7*–*9*). Despite the prevalence of PTLDS, and the increased interest in understanding acute postinfectious syndromes, such as Long Covid, the etiology is not known (*10*, *11*).

Another Lyme disease manifestation that can occur after therapy is postinfectious Lyme arthritis. Lyme arthritis is an inflammatory disorder that is characterized by proliferative synovitis usually affecting one knee. Considerable clinical and basic science data indicate that postinfectious Lyme arthritis is an immune-mediated syndrome because patients are treated effectively with immunosuppressive therapy (*12*). Further, autoimmunity, innate immune responses, and host genetics are central to the severity and resolution of postinfectious Lyme arthritis (*13*, *14*). Spirochetal debris after acute infection is a possible instigator of inflammation, but the molecular identity of the culprits and their ability to persist after infection have remained elusive (*4*, *13*–*16*).

B. burgdorferi is considered a stealth pathogen that is incapable of producing toxins or secreting virulence factors common to other disease-causing bacteria. The Lyme disease spirochete is one of the only known diderms that do not produce the endotoxin lipopolysaccharide (*17*–*19*). These features are at odds with patient symptoms from a clinical perspective. Although many topics in the field are highly debated, it is clear that the disease state is driven by an immune response to the bacterium or bacterial-derived products that become maladaptive in some individuals (*3*–*5*, *12*).

An emerging pathogenic determinant in Lyme disease is the peptidoglycan (PG) cell wall, a molecular sac that protects practically all bacterial cells from bursting from internal osmotic pressure. PG is nearly universal in the bacterial kingdom, where it plays a basic role in cell-envelope homeostasis, but several salient features make *B. burgdorferi* PG (PG^{Bb}) unique. For instance, L-Ornithine (L-Orn) occupies the third position of the PG-stem peptide as the quintessential diamine involved in cross-linking glycan strands in *B. burgdorferi*, rather than the near-ubiquitous *meso*-diaminopimelate (*m*-DAP) or L-Lysine (L-Lys), which is present in most Gram-negative and -positive bacteria, respectively (*16*, *20*, *21*). In addition, *B. burgdorferi* lacks the pathway required for muropeptide (or PG fragment) recycling and sheds ~45% of its entire intracellular PG cell wall out into its extracellular environment per generation (*16*). Another peculiarity is that PG^{Bb} glycan strands terminate with the trisaccharide Glc*N*Ac-Glc*N*Ac-1,6 anhydroMur*N*Ac

[1]Department of Microbiology-Immunology, Feinberg School of Medicine, Northwestern University, Chicago, IL 60611, USA. [2]Human Center for Immunobiology, Feinberg School of Medicine, Northwestern University, Chicago, IL 60611, USA. [3]Department of Biochemistry, Virginia Tech, Blacksburg, VA 24061, USA. [4]Center for Emerging, Zoonotic, and Arthropod-borne Pathogens, Virginia Tech, Blacksburg, VA 24061, USA. [5]Department of Biomedical and Veterinary Medicine, Virginia Tech, Blacksburg, VA 24061, USA. [6]Department of Microbiology and Immunology, Medical College of Wisconsin, Milwaukee, WI 53226, USA. [7]Department of Comparative Medicine, Yale School of Medicine, New Haven, CT 06510, USA. [8]Center for Immunology and Inflammatory Diseases, Massachusetts General Hospital and Harvard Medical School, Boston, MA 02114, USA. [9]Translational Biology, Medicine, and Health, Virginia Tech, Blacksburg, VA 24061, USA.
*Corresponding author. Email: brandon.jutras@northwestern.edu

(G-G-anhM) instead of the canonical Glc*N*Ac-1,6 anhydroMur*N*Ac found in nearly all other bacterial clades (*22*). How these unusual features contribute to the overall pathogenicity of *B. burgdorferi* is not known, but PG^{Bb} can be detected in the synovial fluid attained from the swollen joints of patients with Lyme arthritis during infection and often in patients with postinfectious Lyme arthritis after oral or intravenous antibiotic therapy (*16*). In this study, using a murine model, we created a real-time tracking system to understand the fate of bacterial PG as a function of chemistry in live animals and found a mechanism of antigen persistence that may help explain the pathogenicity of PG^{Bb}.

RESULTS

Polymeric PG^{Bb} persists in the murine liver

PG^{Bb} persistence at the site of Lyme arthritis inflammation after antibiotic therapy raises several questions that could only be addressed with tools that could assess cell wall biodistribution at the organismal level (*16*). We created a strategy in which PG^{Bb} was covalently linked to a functionalized dye and tracked the spatial and temporal dynamics of its distribution in live mice, in real time, and compared our results with those of the same amount of dye alone. BALB/cJ mice were used in this system because they develop moderate arthritis when infected with live *B. burgdorferi*; were previously shown to experience arthritis when injected with PG^{Bb} intravenously; and have skin pigmentation that is amendable to fluorescent molecule tracking. Intravenous, retro-orbital (R.O.) administration of cy5 dye alone resulted in near-ubiquitous signal within hours, which was not the case for cy5:PG^{Bb} (fig. S1). Instead, cy5:PG^{Bb} appeared to rapidly accumulate in the murine liver and spleen (Fig. 1A and fig. S1). Within 2 days, cy5:PG^{Bb} was ~100-fold higher than the dye control in the murine abdomen and could be seen draining from the liver and into the inflamed murine ankle (Fig. 1, A and B, and fig. S1). Ex vivo organ imaging, coupled with arthritis scoring and histology, confirmed that the liver was the primary site of cy5:PG^{Bb} accumulation and that cy5:PG^{Bb} caused both joint/tendon inflammation consistent with unlabeled PG^{Bb} [fig. S2 and (*16*)]. Even after more than 2 weeks postinjection, the cy5:PG^{Bb}-derived signal was >10-fold more than that of dye alone (Fig. 1B).

Acute stages of *B. burgdorferi* infection coincide with rapid growth. *B. burgdorferi* replication results in muropeptide shedding, which could contribute to the pool of persistent PG in humans (*16*, *23*). Periplasmic PG would also be liberated into larger polymeric pieces after antibiotic treatment or cell death during spirochete invasion after tick transmission (Fig. 1C). Because our studies rely on highly purified, native components to produce interpretable results, we opted to mimic each form of PG^{Bb}. Digestion with mutanolysin, an *N*-acetylmuramidase, created labeled PG^{Bb} fragments that simulated released pieces produced during growth (digested or dPG^{Bb}). To produce polymeric PG debris (pPG), we sonicated sacculi to mechanically shear pure cy5.5:PG^{Bb} into larger pieces, which was the same form used for our initial study (Fig. 1, A and B). Despite matching the fluorescent intensity and concentration injected, muropeptide fragments (cy5.5:dPG^{Bb}) were rapidly cleared within 2 days, and signal reached baseline values in 4 days, whereas polymeric PG (cy5.5:pPG^{Bb}) persisted (Fig. 1, D and E). Given our initial findings (Fig. 1B), we extended the length of this study and found that the cy5.5:pPG^{Bb} signal was significantly higher than that of dPG, even after 4 weeks (Fig. 1E, $P < 0.01$). The clearance of cy5.5:dPG^{Bb} fit the model of a one-phase exponential decay ($R^2 = 0.9315$), indicating that dPG^{Bb} was being excreted at a continuous rate, consistent with the amount injected. The dye used in this study, cy5.5, was the same for each cell wall material but differed from studies in Fig. 1 (A and B), which used cy5. This confirms that pPG^{Bb} retention is not an artifact of the dye, but rather an inherent property of the *B. burgdorferi* cell wall (Fig. 1, A to E).

The chemical composition and organization of PG^{Bb} is unique (*16*, *21*, *22*), which made us question whether differences in stem-peptide chemistry affect murine retention or liver accumulation. To assess this possibility, we developed a dual-labeling, tandem tracking system in which two PG preparations can be independently labeled but coinjected into the same animal. Using two dyes with different spectral properties, cy5 and cy5.5, we could unmix the signals produced by each preparation to understand the biodistribution of both at the same time. This strategy controls for variability between both the individual nature of each animal and the payload being delivered. We chose two well-characterized bacterial PG stem peptide types from two bacteria common in the kingdom, *Escherichia coli* (*m*-DAP PG) and *Staphylococcus aureus* (L-Lys PG), covalently labeled them with cy5.5, and coinjected each with cy5:pPG^{Bb}. Polymeric *E. coli* PG (cy5.5:pPG^{Ec}) and *S. aureus* PG (cy5.5:pPG^{Sa}) transiently localized to the liver, but the signal was 5- to 30-fold lower than cy5:pPG^{Bb} (Fig. 1, F and G). Much like dPG^{Bb}, both pPG^{Ec} and pPG^{Sa} reached baseline after 48 hours, and the liver was devoid of signal. Because *E. coli* and *S. aureus* PG preparations were pure, potential co-contaminants were nearly undetectable, and both preparations behaved similarly despite drastically different cell wall architectures; our findings suggested that features unique to PG^{Bb} likely contribute to the extended half-life in the liver (fig. S3).

PG^{Bb} contains L-Orn, a rare diamine in the bacterial cell wall. To determine whether this deviation in stem-peptide chemistry contributes to localization or half-life, we purified, labeled, and mono-injected the PG from *Deinococcus radiodurans*, which contains L-Orn with a di-glycine bridge (*24*). The presence of L-Orn in PG did not affect persistence or tissue distribution because *D. radiodurans* PG was readily cleared, similar to the rate of both pPG^{Ec} and pPG^{Sa} (Fig. 1F and fig. S4). The cumulative, longitudinal analysis indicates that, despite injecting equal amounts, PG^{Bb} is uniquely retained relative to other forms of bacterial PG (Fig. 1G).

Another unusual feature of pPG^{Bb} is that glycan strands terminate with G-G-anhM (*22*). It is still unclear how *B. burgdorferi* produces and incorporates G-G-anhM into the spirochete cell wall, but one mechanism in the tick vector appears to be through the direct utilization of the Glc*N*Ac disaccharide chitobiose, a monomer of chitin (*22*, *25*). Mutant bacteria unable to produce the chitobiose transporter ChbC have altered morphology, motility, and an ~37% reduction in the total amount of G-G-anhM (*22*). To understand whether G-G-anhM contributes to pPG^{Bb} half-life, we performed similar tracking studies with purified pPG isolated from a *chbC* mutant strain. Within 6 hours of injection, there was a significant reduction in signal intensity in mice injected with pPG isolated from the *chbC* mutant (fig. S5, $P < 0.05$). Altered amounts of G-G-anhM affected PG-derived signal intensity throughout the initial phase of tracking, but the signal did not reach baseline, similar to all other forms of bacterial PG tested (Fig. 1G and fig. S5), and lower amounts of PG were omnipresent in the liver, suggesting that the atypical glycan strands of PG^{Bb} may partially contribute to organ localization and persistence.

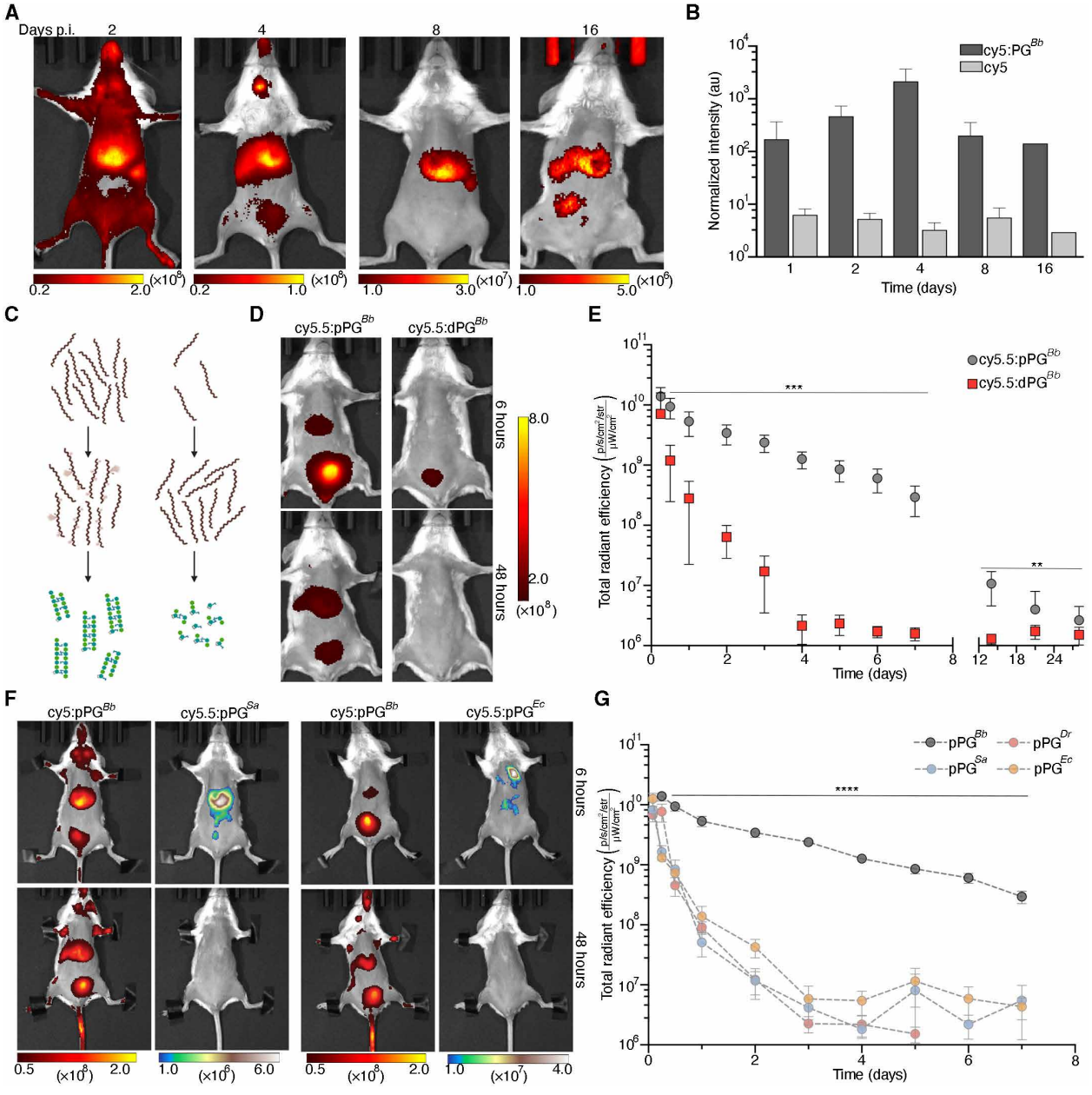

Fig. 1. Polymeric PG^{Bb} persists in the murine liver for weeks. (**A**) PG^{Bb} was covalently labeled with cy5 (cy5:PG^{Bb}), 200 μg of the complex was administered into five mice intravenously by R.O. injection, and the results were compared with those from an equal number of mice injected with matched intensity control (cy5 dye alone). Each group of animals were simultaneously imaged (see fig. S1 for example) at regular intervals using an in vitro imaging system to assess fluorescent signal distribution. Representative images are shown. Heatmaps indicate the total radiant efficiency [(p/s per cm^2 per str)/(μW/cm^2)]. (**B**) The total radiant efficiency of each group described in (A) was calculated on the basis of average value in the abdominal region and normalized by the arm. au, arbitrary units. (**C**) Schematic indicating the two possible sources of free PG^{Bb}. (Left) During the initial stages of infection, *B. burgdorferi* death occurs as a result of transmission, immunological processes, or antimicrobial therapy, leading to polymeric PG release (pPG). (Right) Tick transmission results in population expansion and bacterial cell growth, which causes *B. burgdorferi* to release muropeptide fragments (simulated by dPG). (**D**) Comparative analysis of PG^{Bb} localization and retention after R.O. injection into mice (n = 5 per group) of pPG (cy5.5:pPG^{Bb}), relative to fragments or dPG (cy5.5:dPG^{Bb}) material. Shown are representative mice. Signal intensity was measured 6 hours (top) and 2 days (bottom) postinjection. Heatmap indicates total radiant efficiency [(p/s per cm^2 per str)/(μW/cm^2)]. (**E**) Population-level analysis of cy5.5:pPG^{Bb} signal intensity relative to cy5.5:dPG^{Bb}. The average total radiant efficiency (±SD) was calculated for each group over time (n = 5 per group). Statistical significance was calculated by two-tailed t test; ***P < 0.001 and **P < 0.01 comparing cy5.5:pPG^{Bb} to cy5.5:dPG^{Bb} at each time point. (**F**) Tandem PG localization and retention was measured as a function of chemistry. Polymeric *Staphylococcus aureus* (left) and *Escherichia coli* (right) were purified, cy5.5-labeled (cy5.5:pPG^{Sa} and cy5.5:pPG^{Ec}, respectively), and coinjected (n = 5 per group) with equal amounts of cy5:pPG^{Bb}. Representative mice 6 hours (top) and 2 days (lower) postinjection are shown, as are the total radiant efficiency heatmaps [(p/s per cm^2 per str)/(μW/cm^2)] of each signal. (**G**) Cumulative, average total radiant efficiency values (±SD) are shown for mice shown in (F) and fig. S4 (n = 5 per group). All values attained for pPG^{Bb} were significantly greater than those for all other pPGs tested on and after 12 hours. Data were analyzed by repeated-measures ANOVA; ***P < 0.0001.

PG is retained in Kupffer cells and hepatocytes of mice

Our initial studies indicated that pure PG^{Bb} establishes unique occupancy in the murine liver and that this organ may act as a sink of inflammatory antigen for prolonged periods [Fig. 1; figs. S1, S2, and S5; and (*16*)]. In the well-established murine models of Lyme disease, the liver is not thought to harbor substantial amounts of viable bacteria. If the liver is relevant in retaining pPG^{Bb}, then we would expect to detect PG from dead or dying bacteria in the context of an active infection. We assessed this possibility by needle-inoculating mice with live *B. burgdorferi* and quantified the amount of PG over time using a PG-specific monoclonal antibody. PG^{Bb} was detected in infected animals as early as 1 week after infection (fig. S6). Later stages of infection produced significantly higher amounts of liver-derived PG, but the concentration seemed to plateau and persist after 2 weeks (fig. S6, $P < 0.0001$), suggesting that the liver is a viable sink for PG debris in the context of murine infection.

Hepatocytes and Kupffer cells are the two major cell types in the liver. Hepatocytes are parenchymal cells responsible for macromolecule metabolism, detoxification, and overall liver metabolism (*26*). Kupffer cells are resident liver macrophages whose primary function is to phagocytose foreign viruses, bacteria, and their products before coordinating hepatocyte-mediated excretion in bile (*27*). Given the latter, we hypothesized that pPG was being phagocytosed by Kupffer cells and that differential processing may play a role in pPG^{Bb} persistence. Pulse-chase experiments were performed in which a Kupffer cell line was incubated with cy5:pPG^{Bb}, cy5:pPG^{Ec}, and cy5:pPG^{Sa} to promote phagocytosis; extracellular material was removed with washes; and intracellular pPG signal was tracked over time by flow cytometry. Approximately 90% of all Kupffer cells engulfed cy5-labeled PG, which was expected because of their phagocytic nature (Fig. 2A and fig. S7, $t = 0$). After normalizing for the signal present in each group after uptake, we measured the relative signal intensity present 1 and 2 days later. At each time point, Kupffer cells contained significantly more cy5:pPG^{Bb}-derived signal, relative to cy5:pPG^{Ec} or cy5:pPG^{Sa} (Fig. 2, A and B, $P < 0.001$ for both). Identical studies with intact, labeled, whole cells yielded comparable amounts of *B. burgdorferi* phagocytosis but no discernable difference in intact cell degradation over time, relative to other bacteria (fig. S8). Because each measurement contains more than 10,000 cells and the Kupffer cells appear to be healthy, these data suggest that the PG^{Bb} has a longer intracellular half-life in an immortalized Kupffer cell line (Fig. 2, A to C).

The same studies described above were performed with a hepatocyte cell line. We expected that hepatocytes would be much less active in terms of pPG engulfment relative to Kupffer cells, which was indeed the case (Fig. 2D). One difference, however, was that hepatocytes preferentially engulfed pPG^{Bb} (Fig. 2D). Data collected over three separate experiments indicated that, on average, more than twice as many hepatocytes contained pPG^{Bb} (Fig. 2, D and E). To confirm that phagocytosis was the process by which pPG^{Bb} was being engulfed by hepatocytes, additional studies were performed with increasing concentrations of cytochalasin D and latrunculin A (*28*). We also included a fluorescent bead control that is specifically engulfed by phagocytosis. The percentage of pPG^{Bb}-positive hepatocytes was twice that of even the control, but we also found dose-dependent reduction with phagocytosis-specific inhibitors, confirming the mechanism of endocytosis (Fig. 2E and fig. S9). We extended our findings to once again assess labeled, fixed, and intact cells and found that whole *B. burgdorferi* cells were not phagocytosed by hepatocytes (fig. S10). Together, our studies suggest that pPG^{Bb} is both uniquely engulfed and retained, respectively, in cultured cells involved in liver homeostasis.

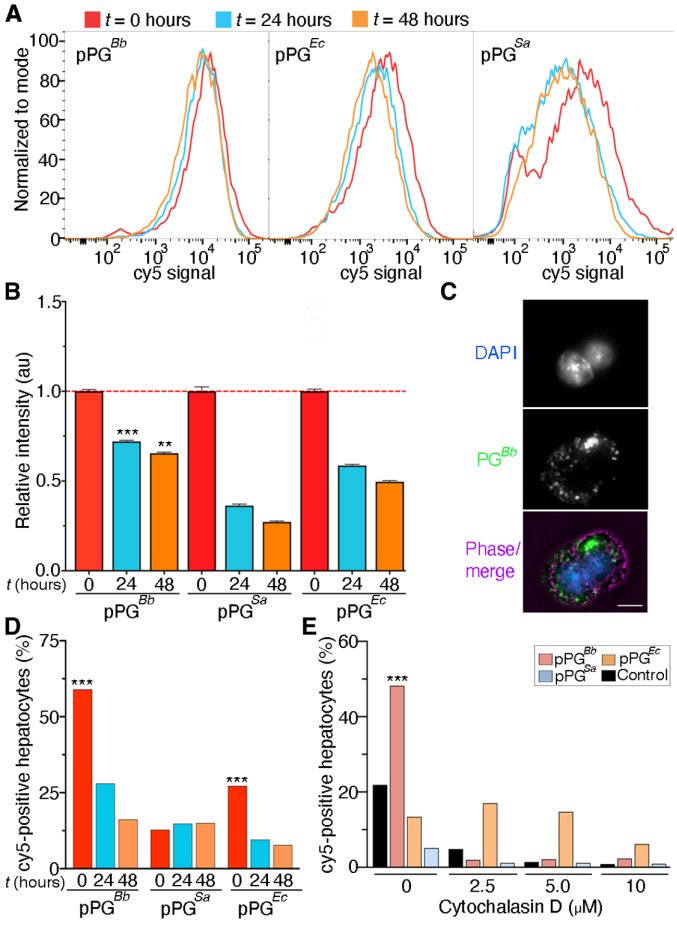

Fig. 2. Hepatocytes and Kupffer cells specifically phagocytose and retain PG^{Bb}, respectively. (**A**) Kupffer cell lines (SCC119) were incubated with cy5-labeled pPG^{Bb}, pPG^{Ec}, or pPG^{Sa} (10 μg/ml). After 24 hours, cells were washed three times to remove extracellular pPG, one sample was removed for analysis ($t = 0$, red), and retention was assessed 24 and 48 hours later (blue and orange, respectively) by flow cytometry. Each time point included >10,000 cells. (**B**) The total intracellular cy5 signal intensity was calculated at $t = 0$ and used to normalize how much signal remained in each experimental condition after 24 and 48 hours. *** indicates that the pPG^{Bb} signal was significantly higher than any other group at the same time point ($P < 0.001$, $n > 10{,}000$ cells, one-way ANOVA with Tukey's correction for multiple comparisons). (**C**) Representative micrographs of SCC119 cells incubated with cy5:pPG^{Bb}. The nucleus (DAPI, top), pPG^{Bb} (cy5, middle), and merge (bottom) are shown. Scale bar, 5 μm. (**D**) Hepatocyte cells (CRL-2390) were incubated with cy5-labeled pPG^{Bb}, pPG^{Ec}, and pPG^{Sa} (10 μg/ml). After 24 hours, cells were washed three times to remove extracellular pPG, and the percentage of cy5-positive cells was assessed by flow cytometry at 0, 24, and 48 hours later (red, blue, and orange, respectively). *** indicates that the pPG^{Bb} signal was significantly higher than any other group at the same time point ($P < 0.001$, chi-square test, $n > 10{,}000$ cells). (**E**) CRL-2390 phagocytosis was assessed by incubating cells with increasing concentrations of cytochalasin D or diluent control (DMSO) for 30 min before incubation with cy5-labeled PGs or the positive control *E. coli* BioParticles. After 24 hours, cells were washed and assayed by flow cytometry, as described above. *** indicates that the pPG^{Bb} signal was significantly higher than any other group at the same time point ($P < 0.001$, chi-square test, $n > 10{,}000$ cells).

PG^{Bb} elicits a unique host response

After establishing that the murine liver acts as a specific sink for pPG^{Bb}, we questioned the underlying consequences at both the tissue and molecular level. Other forms of bacterial PG are rapidly cleared and thus were not considered for subsequent studies. We first examined liver histopathology 35 days after cy5.5:pPG^{Bb} injection and compared our findings with the cy5.5 control (Figs. 1E and 3A). Blind expert scoring indicated that cy5.5:pPG^{Bb} produced minimal gross liver pathology, with some extramedullary hemopoiesis (Fig. 3, A and B). We also assessed potential liver dysfunction by longitudinal serum measurements of both aspartate aminotransferase (AST) and alanine aminotransferase (ALT). AST and ALT concentrations in the experimental and control groups were similar before injection, but 7 days later, both proteins were significantly elevated in cy5.5:pPG^{Bb}-injected mice compared with control mice (Fig. 3C, $P < 0.01$). Serum AST and ALT concentrations peaked at 21 days postadministration and declined afterward but were still elevated after 35 days (Fig. 3C), suggesting that liver dysfunction persists after cy5.5:pPG^{Bb} signal reaches background (Fig. 1E).

All studies thus far have involved labeled pPG^{Bb}. Although the chemical properties of the dye do not affect the outcome (Fig. 1, A, B, D, and E), we sought to further understand the effects of native pPG^{Bb}. We collected sera and organs from animals injected with pPG^{Bb} or diluent 2 days postadministration for further analysis. This interval was selected because all previous studies indicated that only pPG^{Bb} persists at this time point (Fig. 1). In one subset of animals, livers were fixed and probed for unlabeled pPG^{Bb} using immunofluorescence. Compared with phosphate-buffered saline (PBS) control–injected animals, the anti-pPG^{Bb}–derived signal was intense and apparent both within and between cells (Fig. 3D and fig. S11), which further supports liver localization independent of any modification to the PG-stem peptide. In another subset of animals, serum was collected to assess AST and ALT concentrations, and livers were flash-frozen for whole proteome analysis. Both AST and ALT concentrations were elevated, corroborating previous results at an earlier time point (Fig. 3, C and E). The murine liver proteome in animals that received pPG^{Bb} contained signatures that may have broader impacts on physiology and pathogenesis (Fig. 3F). For instance, reactome analysis (*29*) of differentially produced liver proteins after pPG^{Bb} injection indicated that ~70% were associated with innate or adaptive immunity (Fig. 3G). Adaptors and modulators of toll-like receptor (TLR) 1 and TLR2 signaling were dysregulated in the presence of in pPG^{Bb}. An enrichment in processes associated with neutrophil granulation was also apparent (Fig. 3G). Perhaps the most intriguing was that the liver proteome contained signatures common to viral infections. The individual liver proteins altered by pPG^{Bb} were also shown to be dysregulated during severe acute respiratory syndrome coronavirus 2 (SARS-CoV-2) infection and in patients experiencing Long Covid symptoms after infection and apparent virion clearance (tables S1 and S2, $P = 0.00038$).

Host responses to *B. burgdorferi* infection and lingering pPG^{Bb} are important determinants of Lyme disease pathology and resolution (*13*). Because these are driven by maladaptive immunological responses, we considered how human cells from healthy individuals may be altered upon pPG^{Bb} stimulation relative to other types of bacterial PG. Fresh human peripheral blood mononuclear cells (PBMCs) from multiple donors were pooled and stimulated with an equal amount of polymeric, unlabeled PG from multiple sources, in duplicate. Given the scalability of RNA sequencing (RNA-seq), we were able to expand our assessment to include host responses as a function of PG chemistry and include other variants [e.g., *E. coli* (*m*-DAP), *S. aureus* (L-Lys-Gly_5), *Streptococcus mutants* (L-Lys), and *Bacillus subtilis* (amidated *m*-DAP)]. Comparative transcriptomic analysis indicated that more than 10,000 genes were coexpressed upon stimulation with each PG preparation, which makes sense for a common pathogen-associated molecular pattern (PAMP); however, PG^{Bb} caused the greatest number of genes to be significantly differentially expressed (Fig. 3H, $P < 0.01$). One intriguing pattern emerged within these differentially expressed loci; energy metabolism–related genes were among the most differentially expressed (e.g., electron transport chain; tricarboxylic acid, longevity regulating pathway), and most of these genes were specifically down-regulated by pPG^{Bb} (fig. S12, A to C). In addition, C-C motif chemokine ligand 19 (CCL19) and interleukin-23 (IL-23) have been implicated in PTLDS (*30*–*32*), and transcripts for both CCL19 and IL-23 were significantly increased upon pPG^{Bb} stimulation. This immunological response, however, was not specific for a particular type of PG (fig. S12D, $P < 0.0001$). Together, these data suggest a role of lingering *B. burgdorferi* cell wall PG in possibly potentiating chronic symptoms after an acute infection.

Persistent polymeric PG is enriched in synovial samples from individuals with Lyme arthritis

Lyme arthritis is a late-stage disease manifestation that usually occurs months after the initial stages of infection (*13*). In addition, some patients with Lyme arthritis treated with recommended dosages of oral and intravenous antibiotic therapy have persistent synovial inflammation and fibroblast proliferation that may worsen in the postinfectious period (*5*, *12*, *14*, *33*). In these patients, PG^{Bb} was detected exclusively in the synovial fluid of their inflamed joint (*16*). The method used to determine the presence of PG was an enzyme-linked immunosorbent assay (ELISA) using a polyclonal antibody specific for the *B. burgdorferi* cell wall, and, as such, PG was not detectable in the control synovial fluid isolated from patients suffering from other forms of arthritis. Because pPG^{Bb} persists in discrete murine tissues (Fig. 1, A, B, and E) and can be seen in inflamed joints (Fig. 1A), but muropeptide fragments are rapidly excreted (Fig. 1, D and E), we sought to further understand the bioactive molecule in human patients.

We reassessed the previous polyclonal antibody and found it to be specific for PG^{Bb} under a wide range of PG concentrations (fig. S13A), but it could not differentiate pPG^{Bb} from dPG^{Bb} (fig. S13B). To distinguish these forms, we created a monoclonal antibody by vaccinating rabbits with a cocktail of both pPG^{Bb} and dPG^{Bb} and selected B cell clones using functionalized derivatives. One such clone was both highly specific in its affinity for pPG^{Bb} over other types of pPG (Fig. 4A) and could differentiate the polymeric remnants of the *B. burgdorferi* from cell wall fragments created by enzymatic digestion (Fig. 4B). This monoclonal antibody, r-mAb2G10, was used to detect unlabeled PG in mouse livers (fig. S11). We reasoned that it could also be used to delineate which form persists in human Lyme arthritis by ELISA, similar to earlier studies (fig. S6). A subset of human synovial fluid samples collected from patients with either Lyme arthritis or other forms of arthritis (e.g., rheumatoid arthritis, osteoarthritis, and ankylosing spondylitis) was blindly reassessed and decoded after results were attained. Nearly all patients with Lyme arthritis had detectable amounts of pPG^{Bb}, and r-mAb2G10 did not interact with any host components in control samples (Fig. 4C and fig. S13C). r-mAb2G10 detected pPG^{Bb} in 27 of the available 30 samples (90%) attained after oral or

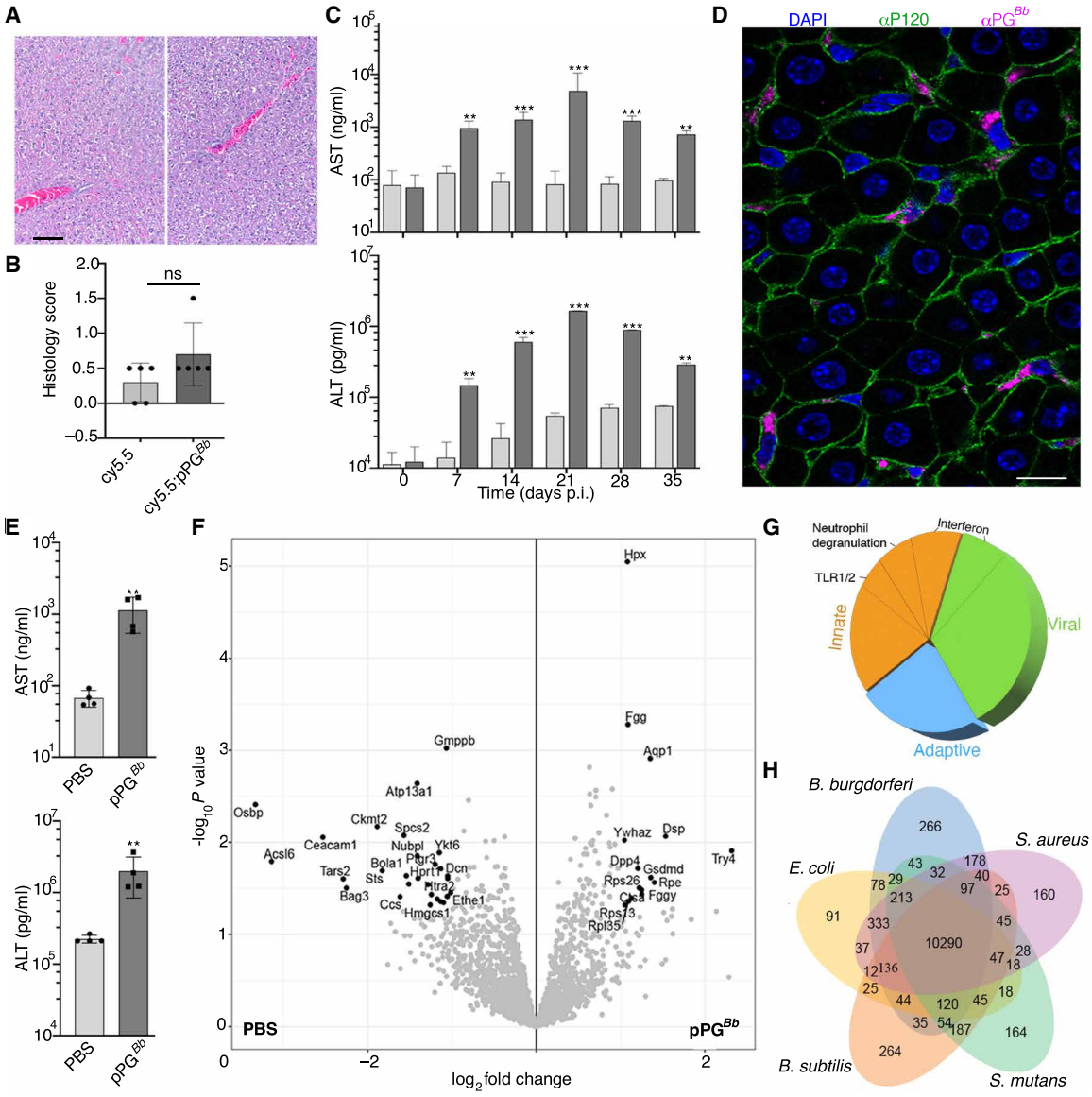

Fig. 3. PG^{Bb} chemistry and persistence alter liver and immunological responses. (**A**) Mouse liver histology was assessed 35 days after cy5.5:pPG^{Bb} (left) or dye control (right). In the cy5.5:pPG^{Bb} image, scant multifocal extramedullary hemopoiesis is apparent. Scale bar, 200 μm. (**B**) Blind histopathological scoring of five mice from each group described in (A) indicates no significant difference (ns). Data are presented as mean ± SD. (**C**) Longitudinal serum analysis of AST (top) and ALT (bottom) concentrations in samples collected from mice in (A) and (B) ($n = 5$ per group). Data were analyzed by unpaired, two-tailed t test for each matching control time point, relative to cy5.5:pPG^{Bb}; $^{**}P < 0.01$ and $^{***}P < 0.001$. days p.i., days postinjection. Data are presented as mean ± SD. (**D**) Mice were injected with unlabeled pPG^{Bb} or PBS control; 2 days postinjection, mice were euthanized, and a subset of the livers were fixed. Immunofluorescence was used to assess the localization of pPG^{Bb} with a recombinant monoclonal antibody (pink), relative to the membrane protein catenin P-120 (green) and nuclei (DAPI, blue). More control and experimental images can be found in fig. S11. Scale bar, 10 μm. (**E**) Serum analysis of AST (upper) and ALT (lower) concentrations in mice ($n = 4$ per group) 2 days after being injected with unlabeled pPG^{Bb} or PBS control. $^{**}P < 0.01$ as measured by two-tailed t test. Data are presented as mean ± SD. (**F**) Volcano plot of the total liver proteome collected from the same experimental groups described in (E) ($n = 3$ biological replicates per group). (**G**) Reactome analysis of significantly affected proteins in (F). Most of the proteins (73.5%) that were both up- and down-regulated by pPG^{Bb} were associated either with innate (orange) and adaptive (blue) immune responses or with viral (green) infection ($P = 0.00038$). Subcategorical enrichment included proteins associated with neutrophil degranulation (9%) or TLR1/2 signaling (8%). Interferon-associated proteins were overrepresented in 8% of both innate immune and viral responses but could not be discretely assigned to one group. (**H**) Venn diagram of transcriptomic analysis of human PBMCs stimulated with purified pPG isolated from different bacteria. Fresh, healthy, human PBMCs were pooled from three donors and stimulated for 12 hours with pPG (50 μg/ml) isolated from *B. burgdorferi* (G-G-anhM/L-Orn-Gly type PG), *E. coli* (*m*-DAP type PG), *S. aureus* (L-Lys-Gly$_5$ type PG), *S. mutans* (L-Lys type PG), or *B. subtilis* (amidated *m*-DAP type PG).

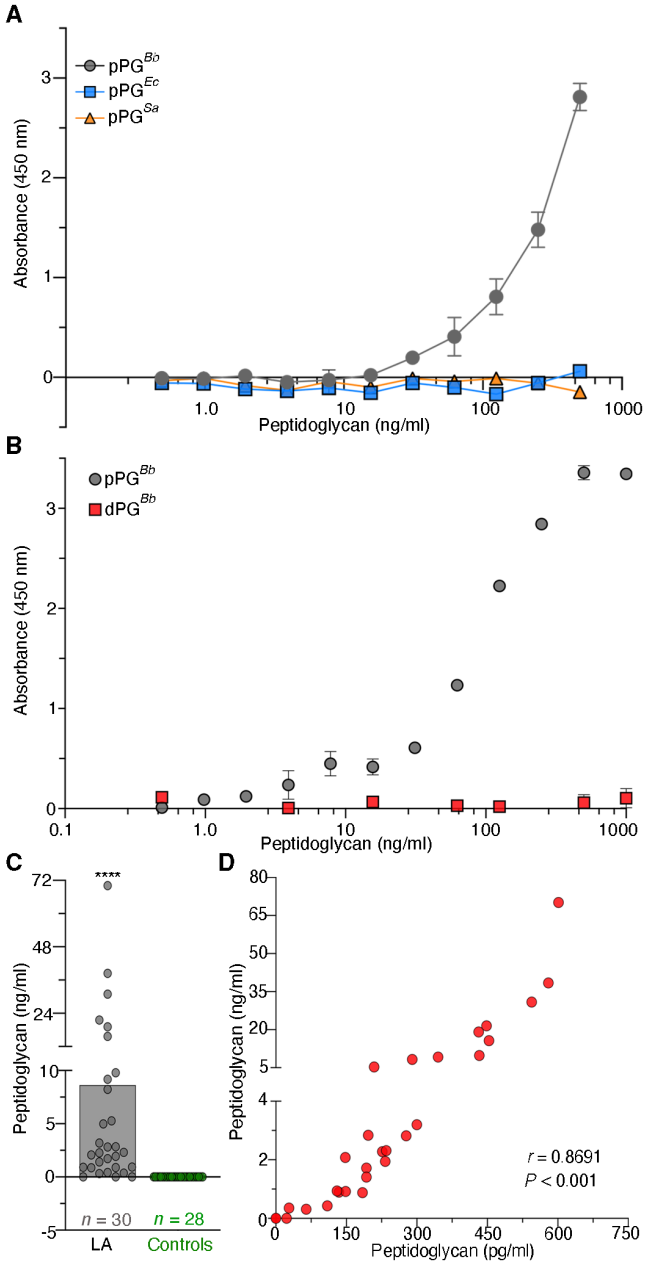

Fig. 4. Polymeric PG^{Bb} persists in patients with Lyme arthritis. (**A**) ELISA was used to determine the specificity of recombinant monoclonal antibody 2G10 (r-mAb2G10). Microtiter plates were coated with r-mAb2G10, followed by incubation with a serial dilution of purified pPG^{Bb} (gray), pPG^{Ec} (blue), or pPG^{Sa} (orange). (**B**) The same assay described in (A) was used to determine the affinity of r-mAb2G10 for pPG^{Bb} (gray) and dPG^{Bb} (red). Data in (A) and (B) are presented as mean ± SD. (**C**) The r-mAb2G10–based ELISA was used to detect pPG^{Bb} in human synovial fluid. Samples from 30 patients with Lyme arthritis (LA) collected at different states of disease and treatment were assayed for the presence of pPG^{Bb}. Control samples included synovial fluid samples collected from patients with rheumatoid arthritis, osteoarthritis, or ankylosing spondylitis. The concentration of PG in each sample was calculated on the basis of standards with known concentrations (see fig. S13). Data were analyzed by Kruskal-Wallis test followed by Dunn's correction, ****$P < 0.0001$. (**D**) Correlation analysis of PG concentrations determined previously, using anti-PG^{Bb} antiserum [(*16*), *x* axis], and those determined using the pPG^{Bb}-specific antibody r-mAb2G10 (*y* axis). Pearson correlation coefficient (*r*) and the corresponding *P* value. Note that the patient samples analyzed in (C) and (D) were a subset of the original study because of sample availability (30 of 34 LA; 28 of 30 controls).

intravenous antibiotic treatment, whereas earlier studies detected PG in 28 of these same 30 samples. It is also relevant to note that the two patient samples that were negative previously were also negative using r-mAb2G10–based pPG^{Bb} detection, meaning that the sensitivity of r-mAb2G10 was 96.4% (Fig. 4C). The calculated concentrations of pPG^{Bb}, although higher in this newly adapted monoclonal antibody-based assay, had a strong correlation with the earlier values attained using the polyclonal antibody (Fig. 4D, $r = 0.8691$). Collectively, our results indicate that polymeric remains of previously intact *B. burgdorferi* sacculi are the bioactive constituents that persist in the synovial fluid of individuals with Lyme arthritis.

DISCUSSION

Here, we tracked PG to understand its fate through the lens of glycochemistry to determine the biodistribution of a ubiquitous bacterial PAMP in real time. Fluorescent signal from cy5:pPG^{Bb} or cy5.5:pPG^{Bb} was above background, and any other type of PG tested, even at 28 days after injection (Fig. 1). In contrast, other types and forms of PG, including muropeptides isolated from *B. burgdorferi*, were rapidly excreted (Fig. 1G). Recent studies are consistent with ours in that PG containing either L-Lys or *m*-DAP, although transiently detectable in the liver, are undetectable by radioisotope labeling within 1 day (*34*). These studies, which used terminal measurements, did not test PG^{Bb} or PG containing L-Orn. To that end, it was unexpected that L-Orn did not contribute to tissue tropism or half-life, as indicated by studies involving *D. radiodurans* PG (fig. S4). In contrast, the retention of pPG^{Bb} that contained reduced amounts of G-G-anhM was lower than wild-type pPG^{Bb}, suggesting that this atypical cell wall trisaccharide may be involved in liver persistence (fig. S5). One source of G-G-anhM is likely tick-derived because trisaccharide concentrations are reduced by 37% when the transport of environmental chitobiose (Glc*N*Ac-Glc*N*Ac) is impaired (*22*, *25*). Endogenous concentrations of chitobiose during vertebrate infection must be exceptionally low, which together suggests that *B. burgdorferi* has yet to be determined mechanism(s) to synthesize G-G-anhM. Future studies should focus on the mechanistic basis of G-G-anhM biosynthesis in *B. burgdorferi* because complete ablation of this unusual glycan modification may eliminate PG persistence.

One function of the liver is to detoxify blood by removing microbes and their products from circulatory systems through the activity of Kupffer cells. Kupffer cells are known to remove *B. burgdorferi* from the blood and phagocytosed bacteria appear to die rapidly (*35*). This is consistent with the notion that the liver is not a prominent site of *B. burgdorferi* replication and, although spirochete DNA may be detected in the organ, viable bacteria are rarely recovered from laboratory strains of mice (*35*–*38*). Our studies suggest that the Kupffer cells readily phagocytose intact *B. burgdorferi* cells and pPG^{Bb}, and the latter persists in contrast to other forms of PG (Fig. 2, A and B). A hepatocyte cell line, on the other hand, did not appear to endocytose intact *B. burgdorferi* cells but was proficient at specifically phagocytosing the spirochete cell wall (Fig. 2, C and D; figs. S9 and S10). Together, it seems plausible to postulate that the liver acts as a sink for pPG^{Bb}, and the two prominent liver cell types serve as specific traps. Kupffer cells engulf live *B. burgdorferi* cells and pPG, whereas hepatocytes phagocytose and retain pPG^{Bb} only. The life span of both hepatocytes and Kupffer cells is difficult to determine in vivo, but experimental data suggest weeks to months (*27*, *39*, *40*). Eventual cell turnover, or acute liver injury and hepatitis, may cause

lingering pPG^{Bb} to transiently re-enter the serum before entering the lymph and synovial fluid. This is supported by the presence of pPG^{Bb} in the synovial fluid of patients with Lyme arthritis even months after therapy and could help explain why patients often experience intermittent attacks of joint pain and swelling (*33*).

Patients with Lyme disease are often treated with an oral regimen of doxycycline and many return to health. Two of the four alternative oral antibiotics recommended to treat Lyme disease, amoxicillin and cefuroxime, target PG synthesis as does intravenous ceftriaxone, which is often used to treat patients with Lyme arthritis who have minimal or no response to oral antibiotics (*3*). In contrast, all beta-lactam treatments would theoretically accelerate the liberation of pPG from the *B. burgdorferi* periplasm. Doxycycline arrests protein synthesis, which would facilitate innate immune system–mediated cell lysis. Together, an obvious question emerges: Why do some patients recover after therapy and others do not? The answer is likely multifactorial and involves the precise interplay between host genetic and autoimmunity, in conjunction with responses to persistent pPG^{Bb}. For instance, polymorphisms in innate immune receptors associated with PG binding are more likely to be found in patients with chronic inflammatory diseases like Crohn's and irritable bowel syndrome (*41*–*43*). Similarly, other cell surface immune receptor polymorphisms are risk factors for postinfectious Lyme arthritis (*13*, *44*–*46*). In these patients, the unusual features of residual pPG^{Bb} may interact with certain polymorphisms in human PG-binding receptors, leading to greater difficulty in clearing PG, proinflammatory immune responses to the debris, and broken immune tolerance (*13*, *16*, *47*). Our liver proteomics studies suggest that the latter two features may indeed occur (Fig. 3, F and G). Such a scenario could involve priming of fibroblast-like synoviocytes by pPG^{Bb}, which can instigate major histocompatibility complex–II antigen presentation to T cells, including presentation of antigens previously associated with autoimmunity in Lyme arthritis (*48*). Another consideration is that the cell wall debris of *B. burgdorferi* may not be the only phlogistic spirochetal remnant in joints. Neutrophil attracting protein A (NapA) can bind to pPG^{Bb}, and NapA has also been detected in the synovial fluid of patients with Lyme arthritis, including in the postinfectious period (*23*, *49*), which, together with PG, may contribute to patient symptomology. By understanding the roles pPG^{Bb} persistence plays in each potential scenario, we may be able to disrupt this entangled web of associations through targeted therapy, allowing patients to return to health without the need for immuno-suppressives or exhaustive antibiotic treatment that may not improve patient symptoms.

The etiology of PTLDS in humans is not known. Efforts to discover metabolic and transcriptomic signatures indicative of PTLDS or predictors of severity have yielded mixed results, but a few candidates have emerged. CCL19 and IL-23, two immunomodulators whose transcripts are up-regulated by PG (fig. S12D), are possible candidates, but clear thresholds to differentiate disease from healthy individuals are lacking (*5*, *12*, *30*–*32*, *50*). Interferon-α is yet another promising prognosticator of PTLDS (*51*). Several modulators of type I interferon responses appeared in our proteome studies, but further studies are needed to confirm a role for interferon-α in PTLDS (Fig. 3G). The lack of validated laboratory markers for PTLDS means that physicians must rely on patient histories, surveys, and qualitative measures such as overall symptoms. A common complaint is chronic fatigue, much like other postacute infection syndromes (*5*–*9*). Therefore, it was interesting to us that many of the specific trans-criptomic responses attributed to the unique features of pPG^{Bb} were associated with energy metabolism (fig. S12, A to C). One caveat is that these data were collected from healthy human PBMCs instead of myocytes, glial cells, or even PBMCs from patients with PTLDS. That said, if our preliminary model above describing transient reentry of pPG^{Bb} into the serum is correct, PBMCs may be temporarily but repeatedly exposed.

Some limitations to our study should be noted. First, our PG tracking studies required R.O. injection to facilitate visualization (Fig. 1). Although PG could be detected in mouse livers after live infection using a different route of inoculation (fig. S6), further method development is required to assess the biodistribution of pPG^{Bb} after tick-mediated transfer of live *B. burgdorferi*, which may affect our results. pPG^{Bb} was also found to accumulate in immortalized Kupffer and hepatocyte cell lines (Fig. 2), but additional studies focusing on primary cells may further define the mechanisms involved in both phagocytosis and persistence. It is also possible that inbred and outbred strains of mice may differ in pPG^{Bb} retention or responses. Of note, a mouse model of PTLDS does not currently exist, so we cannot say the responses truly resemble those found in patients with PTLDS; however, the dysregulated pathways could generate organismal level phenotypes consistent with PTLDS.

The genesis of other postinfectious syndromes such as Long Covid is also unknown, but there seems to be some parallels to PTLDS. For instance, SARS-CoV-2 antigens can persist for months in discrete tissues, but antigen reservoirs are not necessarily the site of pathology (*52*–*56*). Patients with Long Covid have reported experiencing cognitive issues and chronic fatigue, issues that involve mitochondrial dysfunction (*6*, *57*–*63*). Although it is not known if persistent bacterial products are present in the clinically and pathophysiological distinct case of PTLDS, our studies supporting the prolonged residency of a PAMP in distinct organs and cells argue that it is possible and warrants further investigation. Together, these studies may inform our understanding of postinfectious diseases.

MATERIALS AND METHODS

Study design

Our approach to understanding PG^{Bb} persistence involved the quantitative assessment of its biodistribution in live animals, in real time. All animal studies were performed on BALB/cJ in accordance with approved animal welfare and procedures by the Institutional Animal Care and Use Committees (IACUC) of Virginia Tech (nos. 20-051 and 23-099) and the Feinberg School of Medicine, Northwestern University (approval no. A3283-01). Animals were purchased from the Jackson Laboratory at 4 to 6 weeks of age, and studies began when they reached 6 to 8 weeks of age. Power analysis determined the appropriate number of animals in each group; no animals or data points from any study were excluded. End points for each study were either determined on the basis of signal intensity or predefined once methods were repeated. Pathological analysis of liver tissues and arthritis scoring after PG injection were performed blindly. Biological and technical replicates are described for each study in the text or figure legends. Quality control was performed on all materials used in each study and varied depending on the material.

Culture conditions

The murine Kupffer cell line was a gift from W. Maury (University of Iowa), originating from Sigma-Aldrich (SCC119). These cells were grown in RPMI-1640 + 10% fetal bovine serum (FBS) (VWR,

97068–085) and penicillin (100 U/ml)/streptomycin (100 μg/ml) at 37°C with 5% CO_2. Once the cells reached ~90% confluency, they were passaged using cell scrapers to lift the cells. The murine "FL83B" hepatocyte cell line was purchased from the American Type Culture Collection (ATCC; CRL-2390) and cultured in F-12K medium with 10% FBS (not heat inactivated; ATCC #30-2020) with penicillin (100 U/ml)/streptomycin (100 μg/ml) at 37°C and 5% CO_2. To passage, the FL83B cells were washed with sterile PBS and then detached using 3 ml of trypsin EDTA per T-75 flask for ~10 min. The reaction was quenched by adding 8 ml of complete medium, and 2 ml of cell suspension was used to inoculate T-75 flasks.

B. burgdorferi B31-A3, provided by J. Coburn (Medical College of Wisconsin), was grown at 34°C in BSK-II medium supplemented with heat-inactivated 6% rabbit serum to mid-late exponential phase (*64*). *B. burgdorferi* B31-5A3/*chbC1* was grown similarly, but with the addition of gentamycin. This strain was provided by P. Rosa from Rocky Mountain Labs (National Institutes of Health). *E. coli* strain K12, *B. subtilis* 168, and *S. aureus* FDA 209 were grown in Luria-Bertani broth. *D. radiodurans* strain 13939 and *Streptococcus mutans* (Clark) were grown in Tryptone Yeast medium supplemented with 10% glucose and brain-heart infusion medium, respectively. All bacteria but *B. burgdorferi* were grown at 37°C with agitation until the culture reached an optical density at 600 nm (OD_{600}) of 0.5 (Agilent BioTek Synergy H1). Cells were pelleted using centrifugation at 4000*g* for 15 min at 4°C, washed three times with PBS, and frozen at −20°C until needed.

PG isolation and labeling protocol

The methods for PG isolation from bacterial cells were modified from earlier studies (*65*), which were based on Glauner's procedure (*66*). Gram-positive cells were resuspended in PBS and bead beat for 60 s, placed on ice for 60 s, then repeated. Gram-negative cells were resuspended in PBS without undergoing bead beating. Cell suspensions were added dropwise into boiling 10% SDS, resulting in a 5% final concentration. The solution was boiled for 1 hour and then washed five times with warm (~40°C) autoclaved DiH_2O using ultracentrifugation (50,000*g* for 60 min at 30°C). After washing, the PG sacculi were treated with lipase (1 mg/ml) for 3 hours, benzonase nuclease (4 μl/ml) for 2 hours, and chymotrypsin (0.3 mg/ml) overnight with shaking (540 rpm) at 37°C. The next morning, 0.5% SDS (final, v/v) was added, and the samples were heated to 80°C for 30 min before being washed three more times with warm autoclaved DiH_2O using the same conditions as above. PG from Gram-positive bacteria was treated with 1 M HCl for 48 hours while rotating at 4°C. The samples were then ultracentrifuged twice with warmed autoclaved DiH_2O. The purified PG was lyophilized and weighed to determine total yield. It was then resuspended in sterile PBS and labeled with either cy5 or cy5.5 dye (Thermo Fisher Scientific; 62265 and 46418, respectively) using 50 μg of dye per 0.5 mg of PG. The PG and dye were incubated for 1 hour at room temperature with agitation. Unbound dye was removed by washing three times with sterile PBS and then three times with sterile water, centrifuging at 22,000*g* for 10 min. The labeled PG was resuspended in sterile PBS at 2 mg/ml. It was then sonicated for 10 cycles of 1 min of sonication (Branson Sonifier 150, 40% amplitude) followed by 2 min on ice. This was used to generate polymeric PG fragments (pPG). A standard curve of unlabeled cy5 dye was generated to determine the ratio of dye to PG labeling. Soluble muropeptides (dPG) were produced by treating intact sacculi with mutanolysin (62 U/ml final) and 5 μM $NaHPO_4/NaH_2PO_4$, pH 5.5, overnight at 37°C with shaking at 540 rpm. The next morning, an additional amount of mutanolysin was spiked in the same volume as added previously, and the sample was allowed to digest for another 4 to 6 hours. The enzyme was heat-inactivated for 10 min at 100°C, and the sample was centrifuged at 22,000*g* for 30 min to pellet any insoluble material. The supernatant containing digested muropeptides was removed, transferred to a new preweighed tube, and lyophilized. Once the dry weight was determined, the muropeptides were resuspended to the desired concentration in sterile PBS.

Potential LPS contamination in PG preparations was assessed using the manufacturer's recommended conditions (Thermo Fisher Scientific; A39552S). Control *E. coli* lysate was produced by harvesting a 10-ml culture in mid-log exponential growth phase, washing cells with PBS, resuspending in 0.5 ml, and assessing 25 μl after disruption using a bead beater (Bertin Technologies). Standard curves were generated using both formats (micro and macro) and used to determine LPS concentration present in each sample.

In vivo tracking studies

Six- to 8-week-old female BALB/cJ mice were purchased from the Jackson Laboratory and given food and water ad libitum. Mice were anesthetized using vaporized isoflurane for all steps requiring anesthesia. Nair was used for hair removal over regions of interest while mice were anesthetized, at least 1 day before the start of each experiment. HotSnapZ hand warmers wrapped in paper towels were carefully used to keep mice warm during the hair removal process. Only ventral hair was removed for the purposes of two-dimensional epi-illumination imaging. Extra nesting material was also added to each cage to provide additional warmth. The mice were anesthetized, and 100 μl of each fluorescent PG type (2 mg/ml) or 100 μl of unlabeled dye (2.9 μg/ml) was retro-orbitally injected. Mice were anesthetized again and imaged on top of a heated stage at 2, 6, and 12 hours postinjection, then every 24 hours for 1 week. Mice were imaged once a week afterward, all while using the spectral unmixing function set for cy5 or cy5.5 in the Perkin Elmer in vivo imaging system. Throughout experimentation, the mice were scored for arthritis prevalence and severity. Severity was based on a three-point scale assessing ankle diameter, footpad swelling, and overall redness. Prevalence was the percentage of mice in each group who received an arthritis score of $\geq$1. Hair removal touch-ups were performed as needed, roughly once each week. Serum was collected weekly from mice through submandibular bleeds. The blood was incubated at room temperature for 30 min and then spun at 1500*g* for 10 min at 4°C. The supernatant was removed and frozen at −20°C or −80°C until needed. Mice were euthanized using CO_2 asphyxiation followed by cervical dislocation, and tissues were harvested. All image analysis was done using the Living Image Software (version 4.7.3). Briefly, regions of interest were drawn around the ventral cavity of each mouse, and the radiant efficiency was determined using the equation (p/s per cm^2 per str)/(μW/cm^2). For comparisons made to dye-injected control animals, the fluorescent intensity of just the arm was measured as well. The ventral cavity fluorescence was divided by the arm fluorescence to normalize control and experimental groups.

Mouse tissue histopathology and semiquantitative analysis

A subset of mouse rear legs and livers were harvested and fixed in 10% neutral buffered formalin and submitted to the Comparative

Pathology Research Core (Department of Comparative Medicine, Yale University School of Medicine) for blind, comprehensive histopathologic analysis. The tissues were trimmed, decalcified (Decal Solution, limbs only) and processed, embedded in paraffin wax, sectioned, stained with hematoxylin and eosin, and cover-slipped by routine methods. The slides were examined blind to experimental manipulation for histopathologic changes and the limbs scored by semiquantitative analysis for both the presence and severity of inflammation as previously described (*16*, *67*). Liver sections were examined for the presence and severity of hepatitis, necrosis, steatosis, fibrosis, bile duct(ule) hyperplasia bile duct inflammation, and extramedullary hematopoiesis as previously described (*68*, *69*). Slides were analyzed and imaged using an Olympus BX63 Microscope and Olympus DP 28 Camera with Olympus cellSens 4.1 camera software.

Detection of PG^{Bb} in murine livers after live infection

BALB/cJ mice were needle-inoculated (subcutaneously) with 10^4 *B. burgdorferi* cells (or PBS control). Animals were euthanized at 1, 2, and 4 weeks postinfection as described above, and livers were removed and flash-frozen in liquid nitrogen. A portion of each tissue was homogenized with a Precellys (Bertin Technology) bead beater, and undisrupted material was cleared by brief centrifugation. The total protein concentration present in each lysate was calculated by Bradford assay, and the values were used to normalize the PG ELISA values. The same ELISA procedure described below for synovial fluid samples was used to assess PG concentration in mouse livers.

Flow cytometry with immortalized hepatocytes and Kupffer cells

For experimentation, each cell type was seeded in non–TC-treated six-well plates at 1×10^6 cells per well in 1 ml of their respective medium and allowed to adhere overnight. The next day, the cells were incubated with cy5-labeled PG (10 μg/ml), PBS, or cy5-conjugated *E. coli* BioParticles (100 μg/ml; Invitrogen #P35360) as a positive control for phagocytosis in a total volume of 100 μl and incubated for 24 hours. The wells were then washed three times with culture medium to remove any unengulfed PG or BioParticles. One time point was collected immediately after PG removal, and two additional time points were collected 24 and 48 hours after removal of extracellular PG and BioParticles. The Kupffer cells were detached using cell scrapers, and trypsin was used for the hepatocytes (350 μl per well and then 650 μl of medium to quench). The cells were then transferred to 1.5-ml centrifuge tubes and fixed using 4% paraformaldehyde for 30 min with rocking at room temperature, followed by staining with Hoechst (15 μg/ml). Cells were washed three times with PBS by centrifuging at 125*g* for 5 min for the hepatocytes and 500*g* for 3 min for the Kupffer cells. For the retention studies, Hoechst and cy5 were used to gate live cells and cells with PG engulfment, respectively.

For inhibitor studies, cytochalasin D (Sigma-Aldrich #C2618-200UL) or latrunculin A (Abcam #144290) was resuspended in dimethyl sulfoxide (DMSO) to 5 mg/ml and 10 mM, respectively. The compounds were diluted further in DMSO and then added to each well of hepatocytes for 30 min before the addition of fluorescent PG or controls. The same concentration of stimuli was used as described above. After 24 hours, the culture medium was removed, and each well was washed with 1 ml of sterile PBS. The cells were detached and fixed as described above for flow cytometry, with the exception of the Hoechst staining step that was not included.

Assessing phagocytosis of intact cells

All bacterial strains were cultured to mid-log exponential growth phase, harvested, washed in PBS, and fixed with 4% paraformaldehyde. *B. burgdorferi* cells were fixed for 10 min; all other cells were fixed for 30 min before reactions were quenched by placing cells on ice for 20 min. After three washes with PBS, cells were labeled with cy5 N-hydroxysuccinimide (50 μg/ml) for 1 hour with agitation. Unbound dye was removed with four washes of PBS, and both phase contrast and epifluorescent microscopy were used to confirm labeling. A WOLF G2 cell sorter was then used to quantify the cy5 signal intensity within each group of bacteria.

Dishes containing 10^6 Kupffer cells or hepatocytes were incubated with labeled and fixed bacterial cells (5 bacteria:1 eukaryotic cell) for 24 hours. After 24 hours, a sample was removed (time = 0), extracellular bacteria were removed with PBS washes, and additional samples were removed 24 and 48 hours later. Each sample was fixed at the time of collection using methods described above. Flow cytometry (BD FACSymphony A1) was used to quantify intracellular cy5 signal. When appropriate, *E. coli* BioParticles (10, 50, or 100 μg/ml; Invitrogen #P35360) were added as control material.

Tissue immunofluorescence

Livers from murine experiments involving purified PG were fixed overnight with 10% neutral buffered formalin, washed three times with PBS, and then transferred to 70% ethanol until paraffin embedding. Tissues were sliced into 5-μm sections and mounted onto microscope slides. For immunofluorescence, the tissues were deparaffinized in Safeclear followed by decreasing concentrations of ethanol. The antigen retrieval step was performed by incubating the slides for 20 min in 10 mM citric acid buffer, pH 6, heated to 95°C. After cooling, the slides were washed in tris-buffered saline (TBS) and incubated overnight with primary antibodies. Rabbit monoclonal anti-pPG^{Bb} 2G10 (made in collaboration with Abclonal as described below) was used at 7.5 μg/ml, and mouse anti-p120 catenin was used at 10 μg/ml (BD Biosciences #610134). The next day, the slides were washed four times for 5 min each in TBS + 0.025% Triton X-100 (TBS-T) with agitation. Goat anti-rabbit cy5 (7.5 μg/ml; the Jackson Laboratory #111-175-144) and donkey anti-mouse cy3 (1.7 μg/ml; the Jackson Laboratory #715-165-150) secondary antibodies were then incubated for an hour at room temperature in the dark followed by four more wash steps with TBS-T. An autofluorescence quenching kit with DAPI (4′,6-diamidino-2-phenylindole) containing mounting medium was used from Vector labs before sealing the slides (Vector #SP-8500). Slides were imaged using an LMS 880 Indimo Axio Observer confocal microscope (63×/1.40 oil DIC M27 objective) to generate high-quality images. For confocal imaging, the excitation and emission wavelengths used were 405/448, 543/583, and 633/686.

Liver proteomic studies

Sera collected from BALB/cJ mice on day 0 through submandibular bleeds used the same postprocessing conditions listed above. The mice were retro-orbitally injected with 50 μg of unlabeled pPG^{Bb} resuspended in PBS. After 2 days, mice were euthanized as described above, and serum was collected through a cardiac puncture. The liver was rapidly removed and flash-frozen using liquid nitrogen. Next, liver specimens were homogenized in 5% SDS + 50 mM triethylammonium bicarbonate (TEAB), pH 8.5, using a bead beater (Bertin Instrument; Precellys 24 touch) for 7 cycles of 60 s on and 15 s rest at 4500 rpm. The samples were reduced and alkylated using 4.5 mM

dithiothreitol (DTT) and 10 mM iodoacetamide (IAA), respectively; precipitated with methanol; and digested with trypsin (2 μg). After peptide recovery, three biological replicates were run in duplicate using LC-MS/MS.

The data were filtered to remove any hit that had one or fewer peptides present. Fragpipe analyst (20.0 platform with MS Fragger 3.8) was used to reference the *Mus musculus* genome for data analysis with specific advanced criteria selected for. The minimum percentage of non-missing values globally was set to 10, the minimum percentage of non-missing values in at least one condition was set to 60, the differentially expressed (DE) adjusted *P* value cutoff was set to 0.05, and the DE $\log_2$ fold change cutoff was 1. Variance stabilizing normalization, Perseus type imputation, and MaxLFQ intensity were used.

ALT and AST serum quantification

ELISAs were conducted to measure serum concentrations of specific proteins. Mouse AST and ALT ELISA kits were purchased from Abcam (products #ab263882 and #ab282882). Samples were analyzed per the manufacturer's recommendation, and values were attained using the Agilent BioTeK4 synergy H1 microplate reader.

RNA sequencing

Three vials of human PBMCs were purchased from Zen-Bio and pooled together in the provided lymphocyte culture medium. The cells were plated at 2×10^6 cells/ml in 12-well plates and allowed to rest overnight. The cells were then stimulated for 12 hours with purified pPG (50 μg/ml) isolated from *B. burgdorferi*, *E. coli*, *S. aureus*, *B. subtilis*, or *S. mutans* and compared with PBS control. All stimuli and subsequent RNA-seq analysis were performed on biological replicate samples. RNA from pelleted cells was extracted using Trizol reagent and chloroform in combination with an RNA miniprep plus Zymo Research purification kit to remove contaminating DNA. Novogene was responsible for cDNA production, library preparation, and sequencing using Illumina technology. Novogene also performed differential expression analysis, Kyoto Encyclopedia of Genes and Genomes pathway analysis, and Venn diagrams. Their analysis included >39,000,000 clean reads per sample. Clean reads were defined as those that did not contain adapters, and <0.1% of nucleotides in the read could not be determined and had a *Q* score higher than 20.

Monoclonal antibody production

Monoclonal antibody production services were provided by Abclonal. Abclonal was provided with highly purified preparations of PG^{Bb} that were digested using mutanolysin (see above). Instead of removing undigested sacculi, 200 μg of the entire mixture (digested and undigested) was used to vaccinate two New Zealand white rabbits. Animals were boosted with another 200 μg of pPG and dPG each month, for a total of 7 months. After final booster and titer analysis, animals were euthanized, splenocytes were isolated, and individual B cell clones were screened according to Abclonal's procedures. No fewer than 500 clones were tested for affinity toward different forms and types of biotin-conjugated PG^{Bb}. A total of 27 clones were counter-screened using biotin-conjugated *E. coli* and *S. aureus* PG. One such clone had high affinity and specificity for polymeric PG (mAb2G10). The heavy and light chains were cloned into the proprietary TurboCHO viral vector and recombinantly expressed and purified from Chinese hamster ovary (CHO) cells. The latter service was provided by GenScript, yielding a purified, recombinant mAb2G10 (r-mAb2G10).

Determination of mAb2G10 specificity and sensitivity

Sandwich ELISA was used to determine the specificity of r-mAb2G10 for polymeric PG^{Bb}. Briefly, each well of the 96-well plate was coated with 75 μl of r-mAb2G10 (10 μg/ml in 0.05 M carbonate-bicarbonate, pH 9.6) and kept at 4°C overnight with gentle shaking. After washing the plate three times with PBS-T (PBS plus 0.05% Tween 20) to remove unbound antibody, the remaining binding sites were blocked for 1 hour at 37°C using 100 μl of fish serum blocking buffer (Thermo Fisher Scientific). The plate was washed three times and incubated with a titration (1000 to 0.49 ng/ml) of sonicated and digested PG of *B. burgdorferi, E. coli,* or *S. aureus* for 1 hour at 37°C. Unbound material was washed with PBS-T, and the plates were incubated with 75 μl of biotinylated r-mAb2G10 (2 μg/ml in PBS) for 1 hour at 37°C. r-mAb2G10 was biotinylated using Biotin-PEG4-NHS ester (BroadPharm) according to the manufacturer's protocol. After washing, the plates were incubated with horseradish peroxidase (HRP)–conjugated streptavidin (1:10,000; Thermo Fisher Scientific), and bound streptavidin was detected with 1-step ultra TMB-ELISA substrate (Thermo Fisher Scientific) after 15 min of incubation. Stop solution (1.5 N H_2SO_4) was added, and the response was determined by measuring absorbance at 450 nm, after background subtraction of signal attained in the absence of PG (Agilent BioTek H1 Synergy).

Sandwich ELISA was also used to detect PG in synovial fluid. Plates were coated with r-mAb2G10 and blocked as described earlier. Synovial fluid from patients with Lyme arthritis and control samples from patients with rheumatoid arthritis, ankylosing spondylitis, or osteoarthritis were reported earlier (*16*). The plate was incubated with a titration of sonicated PG^{Bb} (1000 to 0.015 ng/ml) for 1 hour at 37°C to create a standard curve. The patient samples were diluted and treated as standards of known concentration. PBS was used as a negative control. All plates were incubated with biotinylated r-mAb2G10 (10 μg/ml in PBS) and HRP-conjugated streptavidin as described above.

Polyclonal antibody specificity and sensitivity for PG^{Bb} using ELISA

The same sandwich ELISA methods described above were used for the originally described polyclonal antibody (*16*), with slight modifications. The primary antibody (poly anti-PG^{Bb}) was diluted 1:40 to coat microtiter plates and capture PG. The same primary was used to detect PG, but at 1:120 dilution, followed by the secondary HRP-conjugated antibody and substrate described above.

Statistical analysis

Individual-level data for experiments where $n < 20$ are presented in data file S1. Most statistical analysis used GraphPad Prism 10.1.2, other previous versions of the same software, or FlowJo VX. Unpaired Student's *t* tests were used to assess statistical significance, and Welch's correction was applied when appropriate (Figs. 1 and 3 and figs. S3, S5, and S6). Analysis of variance (ANOVA) was used to assess statistical significance in datasets containing three or more groups (Fig. 2B and fig. S8). Chi-square tests were applied to the same datasets involving percentages (Fig. 2, C and D). Statistical analysis of pPG present in synovial fluid samples was determined using MatLab scripts available through mathworks and a Kruskal-Wallis

test, followed by Dunn's post hoc correction to account for the assessment of three samples coming from the same patient.

Supplementary Materials

The PDF file includes:
Figs. S1 to S13
Tables S1 and S2
Legend for data file S1
References (*70*–*142*)

Other Supplementary Material for this manuscript includes the following:
Data file S1
MDAR Reproducibility Checklist

REFERENCES AND NOTES

1. K. J. Kugeler, A. M. Schwartz, M. J. Delorey, P. S. Mead, A. F. Hinckley, Estimating the frequency of Lyme disease diagnoses, United States, 2010–2018. *Emerg. Infect. Dis.* **27**, 616–619 (2021).
2. A. M. Schwartz, K. J. Kugeler, C. A. Nelson, G. E. Marx, A. F. Hinckley, Use of commercial claims data for evaluating trends in Lyme disease diagnoses, United States, 2010-2018. *Emerg. Infect. Dis.* **27**, 499–507 (2021).
3. A. C. Steere, F. Strle, G. P. Wormser, L. T. Hu, J. A. Branda, J. W. R. Hovius, X. Li, P. S. Mead, *Lyme borreliosis*, *Nat. Rev. Dis. Primers* **2**, 16090 (2016).
4. J. R. Bobe, B. L. Jutras, E. J. Horn, M. E. Embers, A. Bailey, R. L. Moritz, Y. Zhang, M. J. Soloski, R. S. Ostfeld, R. T. Marconi, J. Aucott, A. Ma'ayan, F. Keesing, K. Lewis, C. B. Mamoun, A. W. Rebman, M. E. McClune, E. B. Breitschwerdt, P. J. Reddy, R. Maggi, F. Yang, B. Nemser, A. Ozcan, O. Garner, D. D. Carlo, Z. Ballard, H.-A. Joung, A. Garcia-Romeu, R. R. Griffiths, N. Baumgarth, B. A. Fallon, Recent progress in Lyme disease and remaining challenges. *Front. Med.* **8**, 666554 (2021).
5. J. N. Aucott, Posttreatment Lyme disease syndrome. *Infect. Dis. Clin. North Am.* **29**, 309–323 (2015).
6. J. N. Aucott, A. W. Rebman, L. A. Crowder, K. B. Kortte, Post-treatment Lyme disease syndrome symptomatology and the impact on life functioning: Is there something here? *Qual. Life Res.* **22**, 75–84 (2013).
7. J. N. Aucott, T. Yang, I. Yoon, D. Powell, S. A. Geller, A. W. Rebman, Risk of post-treatment Lyme disease in patients with ideally-treated early Lyme disease: A prospective cohort study. *Int. J. Infect. Dis.* **116**, 230–237 (2022).
8. L. Geebelen, T. Lernout, B. Devleesschauwer, B. Kabamba-Mukadi, V. Saegeman, L. Belkhir, P. De Munter, B. Dubois, R. Westhovens, Humtick Hospital Group, H. Van Oyen, N. Speybroeck, K. Tersago, Non-specific symptoms and post-treatment Lyme disease syndrome in patients with Lyme borreliosis: A prospective cohort study in Belgium (2016-2020). *BMC Infect. Dis.* **22**, 756 (2022).
9. A. W. Rebman, K. T. Bechtold, T. Yang, E. A. Mihm, M. J. Soloski, C. B. Novak, J. N. Aucott, The clinical, symptom, and quality-of-life characterization of a well-defined group of patients with posttreatment Lyme disease syndrome. *Front. Med.* **4**, 224 (2017).
10. J. Choutka, V. Jansari, M. Hornig, A. Iwasaki, Unexplained post-acute infection syndromes. *Nat. Med.* **28**, 911–923 (2022).
11. H. E. Davis, L. McCorkell, J. M. Vogel, E. J. Topol, Long COVID: Major findings, mechanisms and recommendations. *Nat. Rev. Microbiol.* **21**, 133–146 (2023).
12. A. C. Steere, Posttreatment Lyme disease syndromes: Distinct pathogenesis caused by maladaptive host responses. *J. Clin. Invest.* **130**, 2148–2151 (2020).
13. R. B. Lochhead, K. Strle, S. L. Arvikar, J. J. Weis, A. C. Steere, Lyme arthritis: Linking infection, inflammation and autoimmunity. *Nat. Rev. Rheumatol.* **17**, 449–461 (2021).
14. S. L. Arvikar, A. C. Steere, Diagnosis and treatment of Lyme arthritis. *Infect. Dis. Clin. North Am.* **29**, 269–280 (2015).
15. L. K. Bockenstedt, D. G. Gonzalez, A. M. Haberman, A. A. Belperron, Spirochete antigens persist near cartilage after murine Lyme borreliosis therapy. *J. Clin. Invest.* **122**, 2652–2560 (2012).
16. B. L. Jutras, R. B. Lochhead, Z. A. Kloos, J. Biboy, K. Strle, C. J. Booth, S. K. Govers, J. Gray, P. Schumann, W. Vollmer, L. K. Bockenstedt, A. C. Steere, C. Jacobs-Wagner, *Borrelia burgdorferi* peptidoglycan is a persistent antigen in patients with Lyme arthritis. *Proc. Natl. Acad. Sci. U.S.A.* **116**, 13498–13507 (2019).
17. C. M. Fraser, S. Casjens, W. M. Huang, G. G. Sutton, R. Clayton, R. Lathigra, O. White, K. A. Ketchum, R. Dodson, E. K. Hickey, M. Gwinn, B. Dougherty, J. F. Tomb, R. D. Fleischmann, D. Richardson, J. Peterson, A. R. Kerlavage, J. Quackenbush, S. Salzberg, M. Hanson, R. van Vugt, N. Palmer, M. D. Adams, J. Gocayne, J. Weidman, T. Utterback, L. Watthey, L. McDonald, P. Artiach, C. Bowman, S. Garland, C. Fuji, M. D. Cotton, K. Horst, K. Roberts, B. Hatch, H. O. Smith, J. C. Venter, Genomic sequence of a Lyme disease spirochaete, *Borrelia burgdorferi*. *Nature* **390**, 580–586 (1997).
18. J. D. Radolf, M. J. Caimano, B. Stevenson, L. T. Hu, Of ticks, mice and men: Understanding the dual-host lifestyle of Lyme disease spirochaetes. *Nat. Rev. Microbiol.* **10**, 87–99 (2012).
19. S. Casjens, N. Palmer, R. van Vugt, W. M. Huang, B. Stevenson, P. Rosa, R. Lathigra, G. Sutton, J. Peterson, R. J. Dodson, D. Haft, E. Hickey, M. Gwinn, O. White, C. M. Fraser, A bacterial genome in flux: The twelve linear and nine circular extrachromosomal DNAs in an infectious isolate of the Lyme disease spirochete *Borrelia burgdorferi*. *Mol. Microbiol.* **35**, 490–516 (2000).
20. W. Vollmer, D. Blanot, M. A. de Pedro, Peptidoglycan structure and architecture. *FEMS Microbiol. Rev.* **32**, 149–167 (2008).
21. G. Beck, J. L. Benach, G. S. Habicht, Isolation, preliminary chemical characterization, and biological activity of *Borrelia burgdorferi* peptidoglycan. *Biochem. Biophys. Res. Commun.* **167**, 89–95 (1990).
22. T. G. DeHart, M. R. Kushelman, S. B. Hildreth, R. F. Helm, B. L. Jutras, The unusual cell wall of the Lyme disease spirochaete *Borrelia burgdorferi* is shaped by a tick sugar. *Nat. Microbiol.* **6**, 1583–1592 (2021).
23. M. M. Davis, A. M. Brock, T. G. DeHart, B. P. Boribong, K. Lee, M. E. McClune, Y. Chang, N. Cramer, J. Liu, C. N. Jones, B. L. Jutras, The peptidoglycan-associated protein NapA plays an important role in the envelope integrity and in the pathogenesis of the Lyme disease spirochete. *PLOS Pathog.* **17**, e1009546 (2021).
24. J. C. Quintela, F. García-del Portillo, E. Pittenauer, G. Allmaier, M. A. de Pedro, Peptidoglycan fine structure of the radiotolerant bacterium *Deinococcus radiodurans* Sark. *J. Bacteriol.* **181**, 334–337 (1999).
25. K. Tilly, A. F. Elias, J. Errett, E. Fischer, R. Iyer, I. Schwartz, J. L. Bono, P. Rosa, Genetics and regulation of chitobiose utilization in *Borrelia burgdorferi*. *J. Bacteriol.* **183**, 5544–5553 (2001).
26. J. Gong, W. Tu, J. Liu, D. Tian, Hepatocytes: A key role in liver inflammation. *Front. Immunol.* **13**, 1083780 (2023).
27. A. T. Nguyen-Lefebvre, A. Horuzsko, Kupffer cell metabolism and function. *J. Enzymol. Metab.* **1**, 101 (2015).
28. K. M. DeFife, C. R. Jenney, E. Colton, J. M. Anderson, Disruption of filamentous actin inhibits human macrophage fusion. *FASEB J.* **13**, 823–832 (1999).
29. A. Fabregat, K. Sidiropoulos, G. Viteri, O. Forner, P. Marin-Garcia, V. Arnau, P. D'Eustachio, L. Stein, H. Hermjakob, Reactome pathway analysis: A high-performance in-memory approach. *BMC Bioinformatics* **18**, 142 (2017).
30. J. N. Aucott, M. J. Soloski, A. W. Rebman, L. A. Crowder, L. J. Lahey, C. A. Wagner, W. H. Robinson, K. T. Bechtold, CCL19 as a chemokine risk factor for posttreatment Lyme disease syndrome: A prospective clinical cohort study. *Clin. Vaccine Immunol.* **23**, 757–766 (2016).
31. J. Bouquet, M. J. Soloski, A. Swei, C. Cheadle, S. Federman, J.-N. Billaud, A. W. Rebman, B. Kabre, R. Halpert, M. Boorgula, J. N. Aucott, C. Y. Chiu, Longitudinal transcriptome analysis reveals a sustained differential gene expression signature in patients treated for acute Lyme disease. *mBio* **7**, e00100-e116 (2016).
32. K. Strle, D. Stupica, E. E. Drouin, A. C. Steere, F. Strle, Elevated levels of IL-23 in a subset of patients with post-Lyme disease symptoms following erythema migrans. *Clin. Infect. Dis.* **58**, 372–380 (2014).
33. L. K. Bockenstedt, G. P. Wormser, Review: Unraveling Lyme disease. *Arthritis Rheumatol.* **66**, 2313–2323 (2014).
34. R. Wheeler, P. A. D. Bastos, O. Disson, A. Rifflet, I. Gabanyi, J. Spielbauer, M. Bérard, M. Lecuit, I. G. Boneca, Microbiota-induced active translocation of peptidoglycan across the intestinal barrier dictates its within-host dissemination. *Proc. Natl. Acad. Sci. U.S.A.* **120**, e2209936120 (2023).
35. W. Y. Lee, T. J. Moriarty, C. H. Wong, H. Zhou, R. M. Strieter, N. van Rooijen, G. Chaconas, P. Kubes, An intravascular immune response to *Borrelia burgdorferi* involves Kupffer cells and iNKT cells. *Nat. Immunol.* **11**, 295–302 (2010).
36. K. D. Moody, S. W. Barthold, G. A. Terwilliger, D. S. Beck, G. M. Hansen, R. O. Jacoby, Experimental chronic Lyme borreliosis in Lewis rats. *Am. J. Trop. Med. Hyg.* **42**, 165–174 (1990).
37. T. Masuzawa, Y. Beppu, H. Kawabata, Y. Yanagihara, Y. Iwamoto, T. Shimizu, R. C. Johnson, Experimental *Borrelia burgdorferi* infection of outbred mice. *J. Clin. Microbiol.* **30**, 3016–3018 (1992).
38. J. A. Caine, J. Coburn, A short-term *Borrelia burgdorferi* infection model identifies tissue tropisms and bloodstream survival conferred by adhesion proteins. *Infect. Immun.* **83**, 3184–3194 (2015).
39. G. Steinhoff, K. Wonigeit, C. Sorg, M. Behrend, B. Mues, R. Pichlmayr, Patterns of macrophage immigration and differentiation in human liver grafts. *Transplant. Proc.* **21**, 398–400 (1989).
40. A. W. Duncan, C. Dorrell, M. Grompe, Stem cells and liver regeneration. *Gastroenterology* **137**, 466–481 (2009).
41. A. J. Wolf, D. M. Underhill, Peptidoglycan recognition by the innate immune system. *Nat. Rev. Immunol.* **18**, 243–254 (2018).
42. R. Caruso, N. Warner, N. Inohar, G. Núñez, NOD1 and NOD2: Signaling, host defense, and inflammatory disease. *Immunity* **41**, 898–908 (2014).
43. J. Royet, D. Gupta, R. Dziarski, Peptidoglycan recognition proteins: Modulators of the microbiome and inflammation. *Nat. Rev. Immunol.* **11**, 837–851 (2011).

44. K. Strle, J. J. Shin, L. J. Glickstein, A. C. Steere, Association of a Toll-like receptor 1 polymorphism with heightened Th1 inflammatory responses and antibiotic-refractory Lyme arthritis. *Arthritis Rheum.* **64**, 1497–1507 (2012).
45. N. W. Schröder, I. Diterich, A. Zinke, J. Eckert, C. Draing, V. von Baehr, D. Hassler, S. Priem, K. Hahn, K. S. Michelsen, T. Hartung, G. R. Burmester, U. B. Göbel, C. Hermann, R. R. Schumann, Heterozygous Arg753Gln polymorphism of human TLR-2 impairs immune activation by *Borrelia burgdorferi* and protects from late-stage Lyme disease. *J. Immunol.* **175**, 2534–2540 (2005).
46. T. J. Sellati, B. Sahay, G. P. Wormser, The Toll of a TLR1 polymorphism in Lyme disease: A tale of mice and men. *Arthritis Rheum.* **64**, 1311–1315 (2012).
47. T. Petnicki-Ocwieja, A. S. DeFrancesco, E. Chung, C. T. Darcy, R. T. Bronson, K. S. Kobayashi, L. T. Hu, Nod2 suppresses *Borrelia burgdorferi* mediated murine Lyme arthritis and carditis through the induction of tolerance. *PLOS ONE* **6**, e17414 (2011).
48. J. R. Rouse, R. Danner, A. Wahhab, M. Pereckas, M. E. McClune, A. C. Steere, K. Strle, B. L. Jutras, R. B. Lochhead, HLA-DR-expressing fibroblast-like synoviocytes are inducible antigen presenting cells that present autoantigens in Lyme arthritis. *ACR Open Rheumatol.* **6**, 678–689 (2024).
49. G. Codolo, F. Bossi, P. Durigutto, C. D. Bella, F. Fischetti, A. Amedei, F. Tedesco, S. D'Elios, M. Cimmino, A. Micheletti, M. A. Cassatella, M. M. D'Elios, M. de Bernard, Orchestration of inflammation and adaptive immunity in *Borrelia burgdorferi*-induced arthritis by neutrophil-activating protein A. *Arthritis Rheum.* **65**, 1232–1242 (2013).
50. H. D. Vrijmoeth, J. Ursinus, M. G. Harms, A. D. Tulen, M. E. Baarsma, F. R. van de Schoor, S. A. Gauw, T. P. Zomer, Y. M. Vermeeren, J. A. Ferreira, H. Sprong, K. Kremer, H. Knoop, L. A. B. Joosten, B. J. Kullberg, J. W. Hovius, C. C. van den Wijngaard, Determinants of persistent symptoms after treatment for Lyme borreliosis: A prospective observational cohort study. *EBioMedicine* **98**, 104825 (2023).
51. S. A. Hernández, K. Ogrinc, M. Korva, A. Kastrin, P. Bogovič, T. Rojko, K. W. Kelley, J. J. Weis, F. Strle, K. Strle, Association of persistent symptoms after Lyme neuroborreliosis and increased levels of interferon-α in blood. *Emerg. Infect. Dis.* **29**, 1091–1101 (2023).
52. D. M. Altmann, C. J. Reynolds, G. Joy, A. D. Otter, J. M. Gibbons, C. Pade, L. Swadling, M. K. Maini, T. Brooks, A. Semper, Á. McKnight, M. Noursadeghi, C. Manisty, T. A. Treibel, J. C. Moon, COVIDsortium investigators, R. J. Boyton, Persistent symptoms after COVID-19 are not associated with differential SARS-CoV-2 antibody or T cell immunity. *Nat. Commun.* **14**, 5139 (2023).
53. C. C. L. Cheung, D. Goh, X. Lim, T. Z. Tien, J. C. T. Lim, J. N. Lee, B. Tan, Z. E. A. Tay, W. Y. Wan, E. X. Chen, S. N. Nerurkar, S. Loong, P. C. Cheow, C. Y. Chan, Y. X. Koh, T. T. Tan, S. Kalimuddin, W. M. D. Tai, J. L. Ng, J. G. Low, J. Yeong, K. H. Lim, Residual SARS-CoV-2 viral antigens detected in GI and hepatic tissues from five recovered patients with COVID-19. *Gut* **71**, 226–229 (2022).
54. C. Gaebler, Z. Wang, J. C. C. Lorenzi, F. Muecksch, S. Finkin, M. Tokuyama, A. Cho, M. Jankovic, D. Schaefer-Babajew, T. Y. Oliveira, M. Cipolla, C. Viant, C. O. Barnes, Y. Bram, G. Breton, T. Hägglöf, P. Mendoza, A. Hurley, M. Turroja, K. Gordon, K. G. Millard, V. Ramos, F. Schmidt, Y. Weisblum, D. Jha, M. Tankelevich, G. Martinez-Delgado, J. Yee, R. Patel, J. Dizon, C. Unson-O'Brien, I. Shimeliovich, D. F. Robbiani, Z. Zhao, A. Gazumyan, R. E. Schwartz, T. Hatziioannou, P. J. Bjorkman, S. Mehandru, P. D. Bieniasz, M. Caskey, M. C. Nussenzweig, Evolution of antibody immunity to SARS-CoV-2. *Nature* **591**, 639–644 (2021).
55. A. Fernández-Castañeda, P. Lu, A. C. Geraghty, E. Song, M.-H. Lee, J. Wood, M. R. O'Dea, S. Dutton, K. Shamardani, K. Nwangwu, R. Mancusi, B. Yalçın, K. R. Taylor, L. Acosta-Alvarez, K. Malacon, M. B. Keough, L. Ni, P. J. Woo, D. Contreras-Esquivel, A. M. S. Toland, J. R. Gehlhausen, J. Klein, T. Takahashi, J. Silva, B. Israelow, C. Lucas, T. Mao, M. A. Peña-Hernández, A. Tabachnikova, R. J. Homer, L. Tabacof, J. Tosto-Mancuso, E. Breyman, A. Kontorovich, D. McCarthy, M. Quezado, H. Vogel, M. M. Hefti, D. P. Perl, S. Liddelow, R. Folkerth, D. Putrino, A. Nath, A. Iwasaki, M. Monje, Mild respiratory COVID can cause multi-lineage neural cell and myelin dysregulation. *Cell* **185**, 2452–2468.e16 (2022).
56. R. Yang, J. Feng, H. Wan, X. Zeng, P. Ji, J. Zhang, Liver injury associated with the severity of COVID-19: A meta-analysis. *Front. Pub. Health* **11**, 1003352 (2023).
57. B. Dufrusine, S. Valentinuzzi, S. Bibbò, V. Damiani, P. Lanuti, D. Pieragostino, P. Del Boccio, E. D'Alessandro, A. Rabottini, A. Berghella, N. Allocati, K. Falasca, C. Ucciferri, F. Mucedola, M. Di Perna, L. Martino, J. Vecchiet, V. De Laurenzi, E. Dainese, Iron dyshomeostasis in COVID-19: Biomarkers reveal a functional link to 5-lipoxygenase activation. *Int. J. Mol. Sci.* **24**, 15 (2023).
58. E. M. Sajdel-Sulkowska, Neuropsychiatric ramifications of COVID-19: Short-chain fatty acid deficiency and disturbance of microbiota-gut-brain axis signaling. *Biomed. Res. Int.* **2021**, 7880448 (2021).
59. N. Zhang, S. Wang, C. C. L. Wong, Proteomics research of SARS-CoV-2 and COVID-19 disease. *Med. Rev.* **2**, 427–445 (2021).
60. T. Välikangas, S. Junttila, K. T. Rytkönen, A. Kukkonen-Macchi, T. Suomi, L. L. Elo, COVID-19-specific transcriptomic signature detectable in blood across multiple cohorts. *Front. Genet.* **13**, 929887 (2022).
61. H. N. du Preez, C. Aldous, H. G. Kruger, L. Johnson, N-Acetylcysteine and other sulfur-donors as a preventative and adjunct therapy for COVID-19. *Adv. Pharmacol. Pharm. Sci.* **2**, 4555490 (2022).
62. D. G. May, L. Martin-Sancho, V. Anschau, S. Liu, R. J. Chrisopulos, K. L. Scott, C. T. Halfmann, R. Díaz Peña, D. Pratt, A. R. Campos, K. J. Roux, A BioID-derived proximity interactome for SARS-CoV-2 proteins. *Viruses* **14**, 611 (2022).
63. A. Jabeen, N. Ahmad, K. Raza, Global gene expression and docking profiling of COVID-19 infection. *Front. Genet.* **13**, 870836 (2022).
64. A. G. Barbour, Isolation and cultivation of Lyme disease spirochetes. *Yale J. Biol. Med.* **57**, 521–525 (1984).
65. B. L. Jutras, M. Scott, B. Parry, J. Biboy, J. Gray, W. Vollmer, C. Jacobs-Wagner, Lyme disease and relapsing fever *Borrelia* elongate through zones of peptidoglycan synthesis that mark division sites of daughter cells. *Proc. Natl. Acad. Sci. U.S.A.* **113**, 9162–9170 (2016).
66. B. Glauner, Separation and quantification of muropeptides with high-performance liquid chromatography. *Anal. Biochem.* **172**, 451–464 (1988).
67. J. Dai, P. Wang, S. Adusumilli, C. J. Booth, S. Narasimhan, J. Anguita, E. Fikrig, Antibodies against a tick protein, Salp15, protect mice from the Lyme disease agent. *Cell Host Microbe* **6**, 482–492 (2009).
68. H. W. Stout-Delgado, W. Du, A. C. Shirali, C. J. Booth, D. R. Goldstein, Aging promotes neutrophil-induced mortality by augmenting IL-17 production during viral infection. *Cell Host Microbe* **6**, 446–456 (2009).
69. H. Kim, C. J. Booth, A. B. Pinus, P. Chen, A. Lee, M. Qiu, M. Whitlock, P. S. Murphy, C. T. Constable, Induced hepatic fibrosis in rats: Hepatic steatosis, macromolecule content, perfusion parameters, and their correlations—Preliminary MR imaging in rats. *Radiology* **247**, 696–705 (2008).
70. B. Aryal, J. Tillotson, K. Ok, A. T. Stoltzfus, S. L. J. Michel, V. A. Rao, Metal-induced oxidative stress and human plasma protein oxidation after SARS-CoV-2 infection. *Sci. Rep.* **13**, 2441 (2023).
71. K. E. Ward, L. Steadman, A. R. Karim, G. M. Reynolds, M. Pugh, W. Chua, S. E. Faustini, T. Veenith, R. S. Thwaites, P. J. M. Openshaw, M. T. Drayson, A. M. Shields, A. F. Cunningham, D. C. Wraith, A. G. Richter, SARS-CoV-2 infection is associated with anti-desmoglein 2 autoantibody detection. *Clin. Exp. Immunol.* **213**, 243–251 (2023).
72. X. Liu, S. Ding, P. Liu, The roles of gasdermin D in coronavirus infection and evasion. *Front. Microbiol.* **12**, 784009 (2021).
73. L. Allnoch, G. Beythien, E. Leitzen, K. Becker, F. J. Kaup, S. Stanelle-Bertram, B. Schaumburg, N. Mounogou Kouassi, S. Beck, M. Zickler, V. Herder, G. Gabriel, W. Baumgärtner, Vascular inflammation is associated with loss of aquaporin 1 expression on endothelial cells and increased fluid leakage in SARS-CoV-2 infected golden syrian hamsters. *Viruses* **13**, 639 (2021).
74. X. Gu, S. Wang, W. Zhang, C. Li, L. Guo, Z. Wang, H. Li, H. Zhang, Y. Zhou, W. Liang, H. Li, Y. Liu, Y. Wang, L. Huang, T. Dong, D. Zhang, C. C. L. Wong, B. Cao, Probing long COVID through a proteomic lens: A comprehensive two-year longitudinal cohort study of hospitalised survivors. *EBioMedicine* **98**, 104851 (2023).
75. Y. Li, S. Qin, L. Dong, S. Qiao, X. Wang, D. Yu, G. Gao, Y. Hou, S. Quan, Y. Li, F. Fan, X. Zhao, Y. Ma, G. F. Gao, Long-term effects of Omicron BA.2 breakthrough infection on immunity-metabolism balance: A 6-month prospective study. *Nat. Commun.* **15**, 2444 (2024).
76. A. A. Rizvi, A. Kathuria, W. Al Mahmeed, K. Al-Rasadi, K. Al-Alawi, M. Banach, Y. Banerjee, A. Ceriello, M. Cesur, F. Cosentino, M. Galia, S. Y. Goh, A. Janez, S. Kalra, P. Kempler, N. Lessan, P. Lotufo, N. Papanas, S. D. Santos, A. P. Stoian, P. P. Toth, V. Viswanathan, M. Rizzo, Cardiometabolic Panel of International Experts on Syndemic COVID-19 (CAPISCO), post-COVID syndrome, inflammation, and diabetes. *J. Diabetes Complications* **36**, 108336 (2022).
77. L. Rochette, M. Zeller, Y. Cottin, C. Vergely, GDF15: An emerging modulator of immunity and a strategy in COVID-19 in association with iron metabolism. *Trends Endocrinol. Metab.* **32**, 875–889 (2021).
78. P. Qi, M. Huang, H. Zhu, Exploring potential biomarkers and therapeutic targets of long COVID-associated inflammatory cardiomyopathy. *Front. Med.* **10**, 1191354 (2023).
79. S. Jana, M. R. Heaven, C. B. Stauft, T. T. Wang, M. C. Williams, F. D'Agnillo, A. I. Alayash, HIF-1α-dependent metabolic reprogramming, oxidative stress, and bioenergetic dysfunction in SARS-CoV-2-infected hamsters. *Int. J. Mol. Sci.* **24**, 558 (2023).
80. G. D. Vavougios, SARS-CoV-2 dysregulation of PTBP1 and YWHAE/Z gene expression: A primer of neurodegeneration. *Med. Hypotheses* **144**, 110212 (2020).
81. Y. Zhang, R. Guo, S. H. Kim, H. Shah, S. Zhang, J. H. Liang, Y. Fang, M. Gentili, C. N. O. Leary, S. J. Elledge, D. T. Hung, V. K. Mootha, B. E. Gewurz, SARS-CoV-2 hijacks folate and one-carbon metabolism for viral replication. *Nat. Commun.* **12**, 1676 (2021).
82. C. Greene, R. Connolly, D. Brennan, A. Laffan, E. O'Keeffe, L. Zaporojan, J. O'Callaghan, B. Thomson, E. Connolly, R. Argue, J. F. M. Meaney, I. Martin-Loeches, A. Long, C. N. Cheallaigh, N. Conlon, C. P. Doherty, M. Campbell, Blood-brain barrier disruption and sustained systemic inflammation in individuals with long COVID-associated cognitive impairment. *Nat. Neurosci.* **27**, 421–432 (2024).
83. S. Sarkar, S. Karmakar, M. Basu, P. Ghosh, M. K. Ghosh, Neurological damages in COVID-19 patients: Mechanisms and preventive interventions. *MedComm* **4**, e247 (2023).

84. W. A. Wang, A. Carreras-Sureda, N. Demaured, SARS-CoV-2 infection alkalinizes the ERGIC and lysosomes through the viroporin activity of the viral envelope protein. *J. Cell Sci.* **13**, jcs260685 (2023).
85. J. Y. Wang, M. W. Roehrl, V. B. Roehrl, M. H. Roehrl, A master autoantigen-ome links alternative splicing, female predilection, and COVID-19 to autoimmune diseases. *J. Transl. Autoimmun.* **5**, 100147 (2022).
86. S. Pushalkar, S. Wu, S. Maity, M. Pressler, J. Rendleman, B. Vitrinel, L. Jeffery, R. Abdelhadi, M. Chen, T. Ross, M. Carlock, H. Choi, C. Vogel, Complex changes in serum protein levels in COVID-19 convalescents. *Sci. Rep.* **14**, 4479 (2024).
87. A. Rosa, V. E. Pye, C. Graham, L. Muir, J. Seow, K. W. Ng, N. J. Cook, C. Rees-Spear, E. Parker, M. S. Dos Santos, C. Rosadas, A. Susana, H. Rhys, A. Nans, L. Masino, C. Roustan, E. Christodoulou, R. Ulferts, A. G. Wrobel, C. E. Short, M. Fertleman, R. W. Sanders, J. Heaney, M. Spyer, S. Kjær, A. Riddell, M. H. Malim, R. Beale, J. I. MacRae, G. P. Taylor, E. Nastouli, M. J. van Gils, P. B. Rosenthal, M. Pizzato, M. O. McClure, R. S. Tedder, G. Kassiotis, L. E. McCoy, K. J. Doores, P. Cherepanov, SARS-CoV-2 can recruit a heme metabolite to evade antibody immunity. *Sci. Adv.* **7**, eabg7607 (2021).
88. J. Y. Wang, W. Zhang, V. B. Roehrl, M. W. Roehrl, M. H. Roehrl, An autoantigen-ome from HS-Sultan B-lymphoblasts offers a molecular map for investigating autoimmune sequelae of COVID-19. *Aust. J. Chem.* **76**, 525–557 (2023).
89. S. K. Byeon, A. K. Madugundu, K. Garapati, M. G. Ramarajan, M. Saraswat, M. P. Kumar, T. Hughes, R. Shah, M. M. Patnaik, N. Chia, S. Ashrafzadeh-Kian, J. D. Yao, B. S. Pritt, R. Cattaneo, M. E. Salama, R. M. Zenka, B. R. Kipp, S. K. G. Grebe, R. J. Singh, A. A. Sadighi Akha, A. Algeciras-Schimnich, S. Dasari, J. E. Olson, J. R. Walsh, A. J. Venkatakrishnan, G. Jenkinson, J. C. O'Horo, A. D. Badley, A. Pandey, Development of a multiomics model for identification of predictive biomarkers for COVID-19 severity: A retrospective cohort study. *Lancet Digit. Health* **4**, e632–e645 (2022).
90. K. Yin, M. J. Peluso, X. Luo, R. Thomas, M. G. Shin, J. Neidleman, A. Andrew, K. C. Young, T. Ma, R. Hoh, K. Anglin, B. Huang, U. Argueta, M. Lopez, D. Valdivieso, K. Asare, T. M. Deveau, S. E. Munter, R. Ibrahim, L. Ständker, S. Lu, S. A. Goldberg, S. A. Lee, K. L. Lynch, J. D. Kelly, J. N. Martin, J. Münch, S. G. Deeks, T. J. Henrich, N. R. Roan, Long COVID manifests with T cell dysregulation, inflammation and an uncoordinated adaptive immune response to SARS-CoV-2. *Nat. Immunol.* **25**, 218–225 (2024).
91. L. Wang, D. Western, J. Timsina, C. Repaci, W. M. Song, J. Norton, P. Kohlfeld, J. Budde, S. Climer, O. H. Butt, D. Jacobson, M. Garvin, A. R. Templeton, S. Campagna, J. O'Halloran, R. Presti, C. W. Goss, P. A. Mudd, B. M. Ances, B. Zhang, Y. J. Sung, C. Cruchaga, Plasma proteomics of SARS-CoV-2 infection and severity reveals impact on Alzheimer's and coronary disease pathways. *iScience* **26**, 106408 (2023).
92. A. B. Kahraman, Y. Yıldız, K. Çıkı, I. Erdal, H. T. Akar, A. Dursun, A. Tokatlı, S. Sivri, COVID-19 in inherited metabolic disorders: Clinical features and risk factors for disease severity. *Mol. Genet. Metab.* **139**, 107607 (2023).
93. D. B. Kell, G. J. Laubscher, E. Pretorius, A central role for amyloid fibrin microclots in long COVID/PASC: Origins and therapeutic implications. *Biochem. J.* **479**, 537–559 (2022).
94. H. Yoon, L. S. Dean, B. Jiyarom, V. S. Khadka, Y. Deng, V. R. Nerurkar, D. C. Chow, C. M. Shikuma, G. Devendra, Y. Koh, Single-cell RNA sequencing reveals characteristics of myeloid cells in post-acute sequelae of SARS-CoV-2 patients with persistent respiratory symptoms. *Front. Immunol.* **14**, 1268510 (2024).
95. X. Wang, S. Rimal, I. Tantray, J. Geng, S. Bhurtel, T. P. Khaket, W. Li, Z. Han, B. Lu, Prevention of ribosome collision-induced neuromuscular degeneration by SARS CoV-2-encoded Nsp1. *Proc. Natl. Acad. Sci. U.S.A.* **119**, e2202322119 (2022).
96. A. C. Montezano, L. L. Camargo, S. Mary, K. B. Neves, F. J. Rios, R. Stein, R. A. Lopes, W. Beattie, J. Thomson, V. Herder, A. M. Szemiel, S. McFarlane, M. Palmarini, R. M. Touyz, SARS-CoV-2 spike protein induces endothelial inflammation via ACE2 independently of viral replication. *Sci. Rep.* **13**, 14086 (2023).
97. A. Erb, U. M. Zissler, M. Oelsner, A. M. Chaker, C. B. Schmidt-Weber, C. A. Jakwerth, Genome-wide gene expression analysis reveals unique genes signatures of epithelial reorganization in primary airway epithelium induced by type-I, -II and -III interferons. *Biosensors (Basel)* **12**, 929 (2022).
98. J. Aguado, A. A. Amarilla, A. Taherian Fard, E. A. Albornoz, A. Tyshkovskiy, M. Schwabenland, H. K. Chaggar, N. Modhiran, C. Gómez-Inclán, I. Javed, A. A. Baradar, B. Liang, L. Peng, M. Dharmaratne, G. Pietrogrande, P. Padmanabhan, M. E. Freney, R. Parry, J. D. J. Sng, A. Isaacs, A. A. Khromykh, G. Valenzuela Nieto, A. Rojas-Fernandez, T. P. Davis, M. Prinz, B. Bengsch, V. N. Gladyshev, T. M. Woodruff, J. C. Mar, D. Watterson, E. J. Wolvetang, Senolytic therapy alleviates physiological human brain aging and COVID-19 neuropathology. *Nat. Aging* **3**, 1561–1575 (2023).
99. X. Tang, R. Sun, W. Ge, T. Mao, L. Qian, C. Huang, Z. Kang, Q. Xiao, M. Luo, Q. Zhang, S. Li, H. Chen, W. Liu, B. Wang, S. Li, X. Lin, X. Xu, H. Li, L. Wu, J. Dai, H. Gao, L. Li, T. Lu, X. Liang, X. Cai, G. Ruan, F. Xu, Y. Li, Y. Zhu, Z. Kong, J. Huang, T. Guo, Enhanced inflammation and suppressed adaptive immunity in COVID-19 with prolonged RNA shedding. *Cell Discov.* **8**, 70 (2022).
100. X. Liu, S. Huuskonen, T. Laitinen, T. Redchuk, M. Bogacheva, K. Salokas, I. Pöhner, T. Öhman, A. K. Tonduru, A. Hassinen, L. Gawriyski, S. Keskitalo, M. K. Vartiainen, V. Pietiäinen, A. Poso, M. Varjosalo, SARS-CoV-2-host proteome interactions for antiviral drug discovery. *Mol. Syst. Biol.* **17**, e10396 (2021).
101. X. Cao, V. Nguyen, J. Tsai, C. Gao, Y. Tian, Y. Zhang, W. Carver, H. Kiaris, T. Cui, W. Tan, The SARS-CoV-2 spike protein induces long-term transcriptional perturbations of metabolic genes, causes cardiac fibrosis, and reduces myocardial contractile in obese mice. *Mol. Metab.* **74**, 1101756 (2023).
102. C. A. Labarrere, G. S. Kassab, Glutathione deficiency in the pathogenesis of SARS-CoV-2 infection and its effects upon the host immune response in severe COVID-19 disease. *Front. Microbiol.* **13**, 979719 (2022).
103. G. Leuschner, A. Semenova, C. H. Mayr, T. S. Kapellos, M. Ansari, B. Seeliger, M. Frankenberger, N. Kneidinger, R. A. Hatz, A. Hilgendorff, A. Prasse, J. Behr, M. Mann, H. B. Schiller, Mass spectrometry-based autoimmune profiling reveals predictive autoantigens in idiopathic pulmonary fibrosis. *iScience* **26**, 108345 (2023).
104. H. Wang, P. Yang, K. Liu, F. Guo, Y. Zhang, G. Zhang, C. Jiang, SARS coronavirus entry into host cells through a novel clathrin- and caveolae-independent endocytic pathway. *Cell Res.* **18**, 290–301 (2008).
105. X. Wang, H. Bai, J. Ma, H. Qin, Q. Zeng, F. Hu, T. Jiang, W. Mao, Y. Zhao, X. Chen, X. Qi, M. Li, J. Xu, J. Hao, Y. Wang, X. Ding, Y. Liu, T. Huang, C. Fang, C. Ge, D. Li, K. Hu, X. Ren, B. Zhang, B. Zhang, B. Shi, C. Zhang, Identification of distinct immune cell subsets associated with asymptomatic infection, disease severity, and viral persistence in COVID-19 patients. *Front. Immunol.* **13**, 812514 (2022).
106. J. Y. Wang, W. Zhang, M. W. Roehrl, V. B. Roehrl, M. H. Roehrl, An autoantigen profile of human A549 lung cells reveals viral and host etiologic molecular attributes of autoimmunity in COVID-19. *J. Autoimmun.* **120**, 102644 (2021).
107. P. K. Langston, A. Nambu, J. Jung, M. Shibata, H. I. Aksoylar, J. Lei, P. Xu, M. T. Doan, H. Jiang, M. R. MacArthur, X. Gao, Y. Kong, E. T. Chouchani, J. W. Locasale, N. W. Snyder, T. Horng, Glycerol phosphate shuttle enzyme GPD2 regulates macrophage inflammatory responses. *Nat. Immunol.* **20**, 1186–1195 (2019).
108. L. Rodriguez, P. Brodin, Immune system perturbations in patients with long COVID. *Trends Mol. Med.* **30**, 200–201 (2024).
109. A. Flamier, P. Bisht, A. Richards, D. L. Tomasello, R. Jaenisch, Human iPS cell-derived sensory neurons can be infected by SARS-CoV-2. *iScience* **26**, 107690 (2023).
110. V. Conti, G. Corbi, F. Sabbatino, D. De Pascale, C. Sellitto, B. Stefanelli, N. Bertini, M. De Simone, L. Liguori, I. Di Paola, Long COVID: Clinical framing, biomarkers, and therapeutic approaches. *J. Pers. Med.* **13**, 334 (2023).
111. L. G. F. de Assis BarrosD'Elia Zanella, L. de Lima Galvão, The COVID-19 'Bad Tryp' syndrome: NAD/NADH+, tryptophan phenylalanine metabolism and thermogenesis like hecatomb—The hypothesis of pathophysiology based on a compared COVID-19 and yellow fever inflammatory skeleton. *J. Infect. Dis. Epidemiol.* **8**, 243 (2022).
112. B. A. Rosa, M. Ahmed, D. K. Singh, J. A. Choreño-Parra, J. Cole, L. A. Jiménez-Álvarez, T. S. Rodríguez-Reyna, B. Singh, O. Gonzalez, R. Carrion, L. S. Schlesinger, J. Martin, J. Zúñiga, M. Mitreva, D. Kaushal, S. A. Khader, IFN signaling and neutrophil degranulation transcriptional signatures are induced during SARS-CoV-2 infection. *Comm. Biol.* **4**, 290 (2021).
113. I. Paranjpe, P. Jayaraman, C. Y. Su, S. Zhou, S. Chen, R. Thompson, D. M. Del Valle, E. Kenigsberg, S. Zhao, S. Jaladanki, Proteomic characterization of acute kidney injury in patients hospitalized with SARS-CoV2 infection. *Commun. Med. (Lond).* **3**, 81 (2023).
114. G. Wang, B. Xiao, J. Deng, L. Gong, Y. Li, J. Li, Y. Zhong, The role of cytochrome p450 enzymes in COVID-19 pathogenesis and therapy. *Front. Pharmacol.* **13**, 791922 (2022).
115. J. W. Guarnieri, J. M. Dybas, H. Fazelinia, M. S. Kim, J. Frere, Y. Zhang, Y. Soto Albrecht, D. G. Murdock, A. Angelin, L. N. Singh, Core mitochondrial genes are down-regulated during SARS-CoV-2 infection of rodent and human hosts. *Sci. Trans. Med.* **15**, eabq1533 (2023).
116. J. D. S. Willett, T. Lu, T. Nakanishi, S. Yoshiji, G. Butler-Laporte, S. Zhou, Y. Farjoun, J. B. Richards, Colocalization of expression transcripts with COVID-19 outcomes is rare across cell states, cell types and organs. *Hum. Genet.* **142**, 1461–1476 (2023).
117. T. Jakobi, J. Groß, L. Cyganek, S. Doroudgar, Transcriptional effects of candidate COVID-19 treatments on cardiac myocytes. *Front. Cardiovasc. Med.* **9**, 844441 (2022).
118. W. Ji, L. Chen, W. Yang, K. Li, J. Zhao, C. Yan, C. You, M. Jiang, M. Zhou, X. Shen, Transcriptional landscape of circulating platelets from patients with COVID-19 reveals key subnetworks and regulators underlying SARS-CoV-2 infection: Implications for immunothrombosis. *Cell Biosci.* **12**, 15 (2022).
119. G. Miao, H. Zhao, Y. Li, M. Ji, Y. Chen, Y. Shi, Y. Bi, P. Wang, H. Zhang, ORF3a of the COVID-19 virus SARS-CoV-2 blocks HOPS complex-mediated assembly of the SNARE complex required for autolysosome formation. *Dev. Cell* **56**, 427–442 (2021).
120. D. J. Moreno Fernández-Ayala, P. Navas, G. López-Lluch, Age-related mitochondrial dysfunction as a key factor in COVID-19 disease. *Exp. Gastroenterol.* **142**, 111147 (2020).
121. N. de Souza Xavier Costa, G. R. Júnior, E. C. T. do Nascimento, J. M. de Brito, L. Antonangelo, C. S. Faria, J. S. Monteiro, J. C. Setubal, J. R. R. Pinho, R. V. Pereira, M. Seelaender, G. S. de Castro, J. D. C. C. Lima, R. A. de Almeida Monteiro, A. N. Duarte-Neto, P. H. N. Saldiva, L. F. F. da Silva, M. Dolhnikoff, T. Mauad, COVID-19

induces more pronounced extracellular matrix deposition than other causes of ARDS. *Respir. Res.* **24**, 281 (2023).
122. Y. Uchida, H. Uemura, S. Yamaba, D. Hamada, N. Tarumoto, S. Maesaki, S. Mochida, Significance of liver dysfunction associated with decreased hepatic CT attenuation values in Japanese patients with severe COVID-19. *J. Gastroenterol.* **55**, 1098–1106 (2020).
123. Q. Zhang, P. W. Melchert, J. S. Markowitz, In vitro evaluation of the impact of Covid-19 therapeutic agents on the hydrolysis of the antiviral prodrug remdesivir. *Chem. Biol. Interact.* **365**, 110097 (2022).
124. H. Jang, S. Choudhury, Y. Yu, B. L. Sievers, T. Gelbart, H. Singh, S. A. Rawlings, A. Proal, G. S. Tan, Y. Qian, D. Smith, M. Freire, Persistent immune and clotting dysfunction detected in saliva and blood plasma after COVID-19. *Heliyon* **9**, e17958 (2023).
125. S. Shahbaz, L. Xu, M. Osman, W. Sligl, J. Shields, M. Joyce, D. L. Tyrrell, O. Oyegbami, S. Elahi, Erythroid precursors and progenitors suppress adaptive immunity and get invaded by SARS-CoV-2. *Stem Cell Reports* **16**, 1165–1181 (2021).
126. N. Saheb Sharif-Askari, F. Saheb Sharif-Askari, B. Mdkhana, H. A. Hussain Alsayed, H. Alsafar, Z. F. Alrais, Q. Hamid, R. Halwani, Upregulation of oxidative stress gene markers during SARS-COV-2 viral infection. *Free Radic. Biol. Med.* **172**, 688–698 (2021).
127. A. M. Chaves-Filho, O. Braniff, A. Angelova, Y. Deng, M. E. Tremblay, Chronic inflammation, neuroglial dysfunction, and plasmalogen deficiency as a new pathobiological hypothesis addressing the overlap between post-COVID-19 symptoms and myalgic encephalomyelitis/chronic fatigue syndrome. *Brain Res. Bull.* **201**, 110702 (2023).
128. Y. Cai, D. J. Kim, T. Takahashi, D. I. Broadhurst, H. Yan, S. Ma, N. J. W. Rattray, A. Casanovas-Massana, B. Israelow, J. Klein, C. Lucas, T. Mao, A. J. Moore, M. C. Muenker, J. E. Oh, J. Silva, P. Wong, Yale IMPACT Research team, A. I. Ko, S. A. Khan, A. Iwasaki, Kynurenic acid may underlie sex-specific immune responses to COVID-19. *Sci. Sig.* **14**, eabf8483 (2021).
129. T. V. Huynh, L. Rethi, T. W. Lee, S. Higa, Y. H. Kao, Y. J. Chen, Spike protein impairs mitochondrial function in human cardiomyocytes: Mechanisms underlying cardiac injury in COVID-19. *Cells* **12**, 877 (2023).
130. A. N. Uvarova, E. M. Stasevich, A. S. Ustiugova, N. A. Mitkin, E. A. Zheremyan, S. A. Sheetikov, K. V. Zornikova, A. V. Bogolyubova, M. A. Rubtsov, I. V. Kulakovskiy, D. V. Kuprash, K. V. Korneev, A. M. Schwartz, rs71327024 associated with COVID-19 hospitalization reduces *cxcr6* promoter activity in human $CD4^+$ T cells via disruption of c-Myb binding. *Int. J. Mol. Sci.* **24**, 13790 (2023).
131. K. Peppercorn, C. D. Edgar, T. Kleffmann, W. P. Tate, A pilot study on the immune cell proteome of long COVID patients shows changes to physiological pathways similar to those in myalgic encephalomyelitis/chronic fatigue syndrome. *Sci. Rep.* **13**, 22068 (2023).
132. P. Upadhyai, P. U. Shenoy, B. Banjan, M. F. Albeshr, S. Mahboob, I. Manzoor, R. Das, Exome-wide association study reveals host genetic variants likely associated with the severity of COVID-19 in patients of european ancestry. *Life (BAsel)* **12**, 1300 (2022).
133. A. Ghavasieh, S. Bontorin, O. Artime, N. Verstraete, M. De Demenico, Multiscale statistical physics of the pan-viral interactome unravels the systemic nature of SARS-CoV-2 infections. *Commun. Phys.* **4**, 83 (2021).
134. M. M. Pérez, V. E. Pimentel, C. A. Fuzo, P. V. da Silva-Neto, D. M. Toro, T. F. C. Fraga-Silva, L. G. Gardinassi, C. N. S. Oliveira, C. O. S. Souza, N. T. Torre-Neto, J. C. S. de Carvalho, T. C. De Leo, V. Nardini, M. R. Feitosa, R. S. Parra, J. J. R. da Rocha, O. Feres, F. C. Vilar, G. G. Gaspar, L. F. Constant, F. M. Ostini, A. M. Degiovani, A. P. Amorim, A. L. Viana, A. P. M. Fernandes, S. R. Maruyama, E. M. S. Russo, I. K. F. M. Santos, V. L. D. Bonato, C. R. B. Cardoso, C. A. Sorgi, M. Dias-Baruffi, L. H. Faccioli, ImmunoCOVID Brazilian Research Consortium, Acetylcholine, fatty acids, and lipid mediators are linked to COVID-19 severity. *J. Immunol.* **209**, 250–261 (2022).
135. K. O'Leary, D. Zheng, Metacell-based differential expression analysis identifies cell type specific temporal gene response programs in COVID-19 patient PBMCs. *NPJ Syst. Biol. Appl.* **10**, 36 (2024).
136. Z. Chen, C. Wang, X. Feng, L. Nie, M. Tang, H. Zhang, Y. Xiong, S. K. Swisher, M. Srivastava, J. Chen, Interactomes of SARS-CoV-2 and human coronaviruses reveal host factors potentially affecting pathogenesis. *EMBO J.* **40**, e107776 (2020).
137. E. Wauters, P. Van Mol, A. D. Garg, S. Jansen, Y. Van Herck, L. Vanderbeke, A. Bassez, B. Boeck, B. Malengier-Devlies, A. Timmerman, T. Van Brussel, T. Van Buyten, R. Schepers, E. Heylen, D. Dauwe, C. Dooms, J. Gunst, G. Hermans, P. Meersseman, D. Testelmans, J. Yserbyt, S. Tejpar, W. De Wever, P. Matthys, CONTAGIOUS collaborators, J. Neyts, J. Wauters, J. Qian, D. Lambrechts, Discriminating mild from critical COVID-19 by innate and adaptive immune single-cell profiling of bronchoalveolar lavages. *Cell Res.* **31**, 272–290 (2021).
138. J. Bao, S. Liu, X. Liang, C. Wang, L. Cao, Z. Li, F. Wei, A. Fu, Y. Shi, Y. Shen, X. Zhu, Y. Zhao, H. Liu, L. Miao, Y. Wang, S. Liang, L. Wu, J. Huang, T. Guo, F. Liu, A prediction model for COVID-19 liver dysfunction in patients with normal hepatic biochemical parameters. *Life Sci. Alliance* **6**, e202201576 (2023).
139. I. Paranjpe, P. Jayaraman, C. Y. Su, S. Zhou, S. Chen, R. Thompson, D. M. Del Valle, E. Kenigsberg, S. Zhao, S. Jaladanki, K. Chaudhary, S. Ascolillo, A. Vaid, E. Gonzalez-Kozlova, J. Kauffman, A. Kumar, M. Paranjpe, R. O. Hagan, S. Kamat, F. F. Gulamali, H. Xie, J. Harris, M. Patel, K. Argueta, C. Batchelor, K. Nie, S. Dellepiane, L. Scott, M. A. Levin, J. C. He, M. Suarez-Farinas, S. G. Coca, L. Chan, E. U. Azeloglu, E. Schadt, N. Beckmann, S. Gnjatic, M. Merad, S. Kim-Schulze, B. Richards, B. S. Glicksberg, A. W. Charney, G. N. Nadkarni, Proteomic characterization of acute kidney injury in patients hospitalized with SARS-CoV2 infection. *Comm. Med.* **3**, 81 (2023).
140. P. Sharma, A. K. Pandey, D. K. Bhattacharyya, Determining crucial genes associated with COVID-19 based on COPD findings. *Comput. Biol. Med.* **128**, 104126 (2021).
141. Z. Z. Chen, L. Johnson, U. Trahtemberg, A. Baker, S. Huq, J. Dufresne, P. Bowden, M. Miao, J. A. Ho, C. C. Hsu, C. C. Dos Santos, J. G. Marshall, Mitochondria and cytochrome components released into the plasma of severe COVID-19 and ICU acute respiratory distress syndrome patients. *Clin. Proteomics* **20**, 17 (2023).
142. E. G. Rivera, A. Patnaik, J. Salvemini, S. Jain, K. Lee, D. Lozeau, Q. Yao, SARS-CoV-2/COVID-19 and its relationship with NOD2 and ubiquitination. *Clin. Immunol.* **238**, 109027 (2022).

Acknowledgments: We would like to thank all members of the Jutras lab and K. R. Jutras for constructive review of this manuscript. We would like to thank the Fralin Life Sciences Mass Spec Incubator and Flow Cytometry core for assistance. **Funding:** This work was supported by National Institutes of Allergy and Infectious Diseases grant R21AI159800 (to B.L.J.); National Institutes of Allergy and Infectious Diseases grant R01AI173256 (to B.L.J. and R.B.L.); National Institutes of Allergy and Infectious Diseases grant R01AI178711 (to B.L.J. and R.B.L.); the Steven & Alexandra Cohen Foundation (to B.L.J. and M.E.M.); the Global Lyme Alliance (to B.L.J.); and Department of Defense grant TB220039 (to B.L.J. and O.E.). Monoclonal antibody production was supported by an award to B.L.J. from the Bay Area Lyme Foundation. **Author contributions:** M.E.M., O.E., and B.L.J. conceptualized the study. M.E.M., O.E., and B.L.J. developed the methodology. M.E.M., O.E., J.M.D., M.M.D., J.D.T., R.B.L., C.J.B., A.C.S., and B.L.J. performed experiments. B.L.J. and R.B.L. acquired funding and performed project administration. B.L.J. supervised the project. M.E.M., A.C.S., and B.L.J. wrote the original draft of the manuscript. M.E.M., O.E., J.M.D., M.M.D., J.D.T., C.J.B., and R.B.L. reviewed and edited the manuscript. **Competing interests:** The authors declare that they have no competing interests. **Data and materials availability:** All data associated with this study are present in the paper or the Supplementary Materials. Raw transcriptomic data have been deposited as a BioProject under the accession number PRJNA1241737. mAb210 is available upon completion of a material transfer agreement. Contact B.L.J. for more details.

Submitted 24 June 2024
Resubmitted 27 January 2025
Accepted 6 March 2025
Published 23 April 2025
10.1126/scitranslmed.adr2955

Abstract

One-sentence summary: Polymeric *Borrelia burgdorferi* peptidoglycan cell wall can persist in murine livers for weeks to months after direct injection or infection.

Editor's summary

As the tick vector for *Borrelia burgdorferi* expands its range, more individuals are at increased risk of both acute Lyme disease (caused by *B. burgdorferi* infection) and postacute sequelae after Lyme disease. In a pair of papers, Gabby *et al.* and McClune *et al.* expand our knowledge of *B. burgdorferi* with the goal of combatting Lyme disease. Gabby *et al.* posited that antibiotics other than high-dose doxycycline may be able to specifically kill *B. burgdorferi*. They found that a beta-lactam, piperacillin, could eliminate *B. burgdorferi* in vitro and in mice (notably without affecting the microbiome) and provided the mechanistic basis of this activity. McClune *et al.* investigated how the *B. burgdorferi* peptidoglycan (PG^{Bb}) may drive long-term consequences of Lyme disease. They observed that a particular form of PG^{Bb} could persist in the mouse liver for much longer than others, or even peptidoglycan from different bacteria, suggesting that PG^{Bb} could serve as a source of continuous antigen, thereby driving inflammation. Altogether, these studies highlight the need to clear *B. burgdorferi* to avoid persistent PG^{Bb} and provide another antibiotic that may be able to do so. —Courtney Malo